Evaluation of aerosol microphysical, optical and radiative properties measured from a multiwavelength photometer

Yu Zheng[1], Huizheng Che[1], Yupeng Wang[2], Xiangao Xia[3], Xiuqing Hu[4], Xiaochun Zhang[5], Jun Zhu[6], Jibiao Zhu[1], Hujia Zhao[7], Lei Li[1], Ke Gui[1], Xiaoye Zhang[1]

5 [1]State Key Laboratory of Severe Weather & Key Laboratory of Atmospheric Chemistry, Chinese Academy of Meteorological Sciences, China Meteorological Administration, Beijing, 100081, China
[2]Changchun Institute of Optics, Fine Mechanics and Physics, Chinese Academy of Sciences, Changchun, 130033, China
[3]LAGEO, Institute of Atmospheric Physics, Chinese Academy of Sciences, Beijing, 100029, China
[4]National Satellite Meteorological Center, China Meteorological Administration, Beijing, 100081, China
10 [5]Centre for Atmosphere Watch and Services, Meteorological Observation Centre, China Meteorological Administration, Beijing, 100081, China
[6]Jiangsu Key Laboratory of Atmospheric Environment Monitoring and Pollution Control, Collaborative Innovation Center of Atmospheric Environment and Equipment Technology, School of Environmental Science and Engineering, Nanjing University of Information Science & Technology, Nanjing, 210044, China
15 [7]Institute of Atmospheric Environment, China Meteorological Administration, Shenyang 110166, China

Correspondence to: Huizheng Che (chehz@cma.gov.cn)

Abstract. An evaluation of aerosol microphysical, optical and radiative properties measured from a multiwavelength photometer, named CW193, was proposed in this study. The instrument has a highly integrated design, smart control performance, and is composed of three parts (optical head, robotic drive platform, and stents system). Based on the
20 synchronous measurements, the CW193 products was validated using reference data from the AERONET CE318 photometer. The results show that the raw digital counts from CW193 agree well the counts from AERONET ($R > 0.989$), with daily average triplets of around 1.2% to 3.0% for the ultraviolet band and less than 2.0% for the visible and infrared bands. A good aerosol optical depth agreement ($R > 0.997$, 100% within expected error) and root mean square error (RMSE) values ranging from 0.006 (for the 870 nm band) to 0.016 (for 440 nm the band) are obtained, with a relative mean bias (RMB) ranging from
25 0.922 to 1.112 and an aerosol optical depth bias within ±0.04. The maximum deviations of peak value for fine-mode particles varied from about 8.9% to 77.6%, whereas the variation for coarse-mode particles was about 13.1% to 29.1%. The deviation variations of the single scattering albedo were approximately 0.1−1.8%, 0.6−1.9%, 0.1−2.6%, and 0.8−3.5% for the 440 nm, 675 nm, 870 nm, and 1020 nm bands, respectively. For the aerosol direct radiative forcing, deviations of approximately 4.8−12.3% was obtained at the Earth's surface and 5.4−15.9% for the top of the atmosphere. In addition, the water vapor
30 retrievals showed a satisfactory accuracy, characterized by a high R value (~0.997), a small RMSE (~0.020), and good expected error distribution (100% within expected error). The water vapor RMB was about 0.979 and the biases mostly varied within ±0.04, whereas the mean values were concentrated within ±0.02.

1 Introduction

Atmospheric aerosols have a substantial impact on the whole environment, and affect the regional air quality and global climate change in particular. In terms of Earth's climate, aerosols are one of the determining factors for climate change with large uncertainties (Che et al., 2019a; Gui et al., 2017; Hansen et al., 1997; Letu et al., 2020b; Xing et al., 2020; Zhao et al., 2021a). Specifically, atmospheric aerosols can disturb Earth's radiative budget and modify it not only by scattering and/or absorbing the incident solar radiation and the outgoing radiation from the surface (aerosol direct radiative effects) but also by altering the microphysical properties of clouds, such as cloud condensation nuclei concentration and reflectivity (Charlson et al., 1992; Dubovik et al., 2002; Letu et al., 2020a; Zhao et al., 2020). In addition, the distribution of aerosols in the atmosphere is not uniform, and is characterized by high spatial and temporal variability among regions (Gui et al., 2021a; Li et al., 2020a; Zhao et al., 2021b). For these reasons, an integrated and accurate understanding of aerosol microphysical, optical, and radiative properties is essential for studies on the climatic and environmental effects of aerosols, particularly for assessing the response of the climate to anthropogenic aerosols (Bi et al., 2014; Che et al., 2019c; Holben et al., 1998; Miao et al., 2021). At present, the two main techniques used to monitor the variation of columnar aerosol optical properties are remote sensing by satellites and ground-based observations. As revealed by previous studies, the aerosol optical depth (AOD) and Ångström exponent are the most common and important parameters for the aerosol features, and are widely used in numerical modelling and satellite calibration (Li et al., 2020b; Zhang et al., 2021a, 2021b; Zhao et al., 2018).

Remote sensing from satellite-borne platforms has developed rapidly since its inception, owing to its powerful features and convenience, especially for the global and long-term observation of atmospheric aerosols (Gui et al., 2019, 2021c; Ma et al., 2021). For example, The Advanced Very High Resolution Radiometer (AVHRR) (Hauser et al., 2005; Stowe et al., 1997) and the Total Ozone mapping Spectrometer (TOMS) (Hsu et al., 1999) have provided long-term global AOD products from 1979 to the present. The Sea-viewing Wide Field-of-view Sensor (SeaWiFS) and the Visible Infrared Imaging Radiometer Suite (VIIRS) provide aerosol retrieval products such as the fine-mode fraction and the particle densities of aerosols (Gordon and Wang, 1994; Sayer et al., 2012). In recent years, a series of advanced satellite sensors for aerosol monitoring have been launched, such as the Multi-angle Imaging Spectro Radiometer (MISR) (Garay et al., 2017), the Moderate Resolution Imaging Spectrometer (MODIS) (Wei et al., 2019), and the Cloud-Aerosol Lidar and Infrared Pathfinder Satellite Observations (CALIPSO) (Kim et al., 2018), which have contributed greatly to our understanding of the temporal and spatial distribution characteristics of aerosols. Nevertheless, as Li et al (2020a) reported, there are still considerable uncertainties in the satellite AOD retrieval products due to the influence of sensor calibration, cloud contamination, and surface albedo. In addition, owing to the limitation of the temporal resolution of satellite-borne platforms over a specific region, such as high-altitude areas and huge-emission areas, satellite AOD retrieval products cannot meet the advanced requirements for ecological environment assessment, heath effect study and real time monitoring. (Dubovik et al., 2006; Gui et al., 2021b; Ma et al., 2021; Miao et al., 2019; Ningombam et al., 2021; Xing et al., 2021b; Zheng et al., 2019).

For these reasons, aerosol detection from ground-based observations is regarded as the most direct, accurate, and effective technique to measure and study the columnar microphysical, optical, and radiative properties of atmospheric aerosols, and there are extensive ground-based monitoring networks across the world dedicated to aerosol detection, such as the Precision Filter Radiometer (PFR) network of The Global Atmosphere Watch program of the World Meteorological Organization (WMO-GAW; (Cuevas et al., 2019)), the China Aerosol Remote Sensing NETwork (CARSNET; (Che et al., 2015, 2018), the Aerosol Robotic Network (AERONET; (Holben et al., 1998), the PHOtométrie pour le Traitement Opérationnel de Normalisation Satellitaire (PHOTONS; (Goloub et al., 2008), and the SKYrad Network (SKYNET; (Nakajima et al., 2020), all consisting of precise instruments with the 0.02 AOD accuracy suggested by the WMO (Che et al., 2009). Most of these observation networks are equipped with the CE318, an automatic multiband Sun photometer (Cimel Electronique, France), as the master and/or observation instrument, to provide long-term data on the aerosol microphysical, optical, and radiative characteristics on the global scale. These networks have an important role in determining the climatic and environmental effects of aerosols, especially in polar and plateau regions, where the robotic measurements could be a better choice due to the harsh climatic condition and lack of manpower support, and the measurement results have been strictly verified under a wide range of conditions (Dubovik et al., 2000; Eck et al., 1999; Xing et al., 2021a; Zhuang et al., 2017). As reported by WMO-GAW's report No. 162, 207, 227 and 228 (2004, 2012; 2016; 2017), the multiwavelength aerosol optical depth (AOD) is still recommended as the long-term measurement variables at the implementation plan from 2016 to 2023. Particularly via ground based AOD attenuation observation, it is regarded as the highly accurate monitoring method to provide indispensable data for satellites validation and global modelling. According to this guideline, an absolute limit to the estimated uncertainty of 0.02 optical depths for acceptable data and <0.01 as a goal to be achieved in the near future. Additionally, the international coordination of AOD networks is still inadequate and could be improved by a federated network under the WMO-GAW umbrella, and networks should become traceable and maintainable via intercomparisons and calibrations. These guidelines highlighted that data assessment is as important as the field observation. However, in China, due to the vast territory and various landform, there are still many observation gaps in aerosol optical properties monitoring. Furthermore, the complicated underlaying surface and emission condition result in the distinct temporal and spatial variations of aerosol. Therefore, referring to WMO-GAW's criterion, conducting field observation and data evaluation is of great importance to reduce the uncertainties of aerosol optical properties, which will be a great assistance to combat climate change.

So far, except for CE318, POM-02 (Nakajima et al., 2020) and PFR (Kazadzis et al., 2018), there are many photometers have realized the function of AOD measurement in China, such as DTF-5 and PSR-2 (Li et al., 2012; Huang et al., 2019). However, we suggest that all the instruments and their products should meet the WMO-GAW's criterion and keep consistency with AERONET, providing comprehensive, comparable aerosol optical products. Here we present a highly integrated multiwavelength photometer named CW193 (CW means Chinese device for World) for monitoring aerosol microphysical, optical, and radiative properties. It has a user-friendly instruction system, and most of the components are assembled in a

100 robotic drive platform, which makes the whole system efficient and highly integrated. By using direct Sun and diffuse-sky radiation measurements, the CW193 not only provides the columnar instantaneous AOD but also gives detailed information on the aerosol characteristics, including, but not limited, to the volume size distribution (VSD), the single scattering albedo (SSA), the asymmetry factor (ASY), and the aerosol direct radiative forcing (ADRF), which are the key input parameters for numerical models (Miao et al., 2020; Stier et al., 2005; Wang et al., 2013). These features make the CW193 a particularly

105 suitable multiwavelength photometer for monitoring aerosol microphysical, optical, and radiative properties, which is contribute to verifying the satellite and modelling products.

For this study, synchronous measurements were conducted between CW193 and CE318s from AERONET and CARSNET at CAMS (Chinese Academy of Meteorological Sciences), and the products of CW193 were evaluated and compared in detail

110 with the reference of AEROENT, aiming at keeping consistency with it. Following this introduction, the observation site and ancillary information for this study are introduced in section 2. In section 3, a description of the new CW193 multiwavelength photometer is provided. Section 4 provides an evaluation and comparison of the aerosol microphysical, optical, and radiative properties from CW193. Finally, the main conclusions are presented in section 5.

2 Observation site and ancillary information

115 ### 2.1 Observation site

In this study, the CW193 instrument has been tested in the atmospheric composition observation platform of CAMS (116.317 °E, 39.933 °N, 106 m a.s.l., see Figure 1), in the north urban area of Beijing, where the main pollutions are derived from urban activities. As revealed by Che et al. (2015, 2019b) and Zheng et al. (2019), according to long-term ground-based aerosol measurements at CAMS, the annual mean $AOD_{440 nm}$ is ~0.65±0.60, with a maximum monthly mean of ~0.82±0.77 in

120 July and a minimum monthly mean of ~0.39±0.41 in December, which are considered to be representative of the urban atmospheric conditions in China and a good test environment for CW193. The CAMS site is part of the AERONET observation network (named "Beijing-CAMS") and has provided the AOD and other inversion products since its establishment in 2012. In addition, Beijing-CAMS is a transfer Sun calibration site for CARSNET, with the master instruments sent to the Izaña Observatory (Izaña, Canary Islands, Spain; 28.3° N, 16.5° W, 2373 m a.s.l.) for annual calibration. The data of particulate

125 matter (PM) concentrations used in this study were provided by Ministry of Ecology and Environment of the People's Republic of China (https://air.cnemc.cn:18007/).
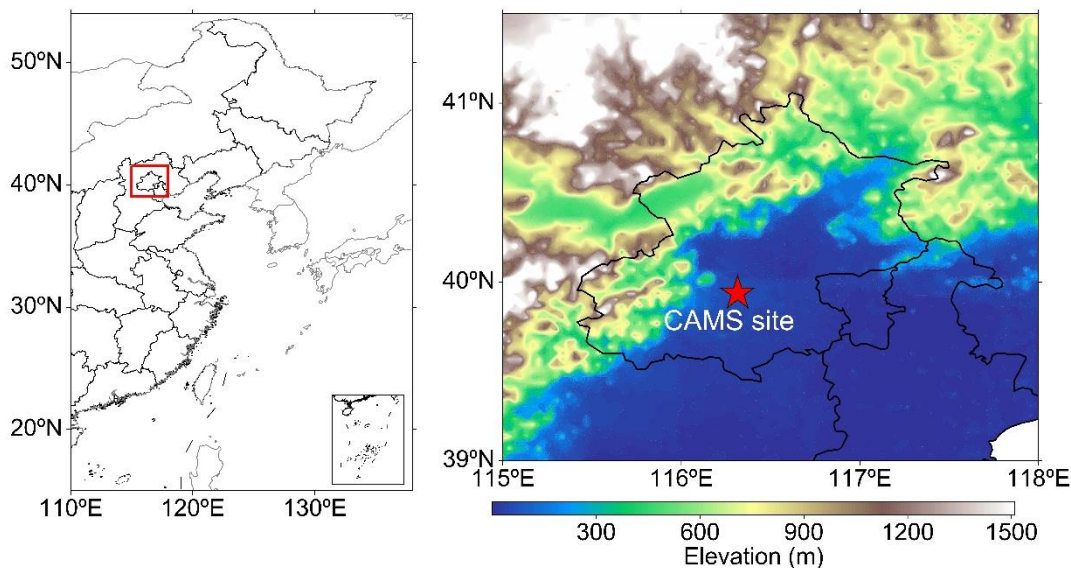
Figure 1. Location of the CAMS site.

130

2.2 Ancillary information

2.2.1 CE318 Sun photometer and its observation network

In this comparative observation campaign, the AOD data and their correlative aerosol inversions provided by AERONET and CARSNET were used to validate the results retrieved from the CW193 observations. AERONET is the biggest federated

135 instrument network in the world, providing open-access data for aerosol microphysical, optical, and radiative properties (https://aeronet.gsfc.nasa.gov/). CARSNET is the largest ground-based aerosol remote-sensing network in China, with more than 80 sites in China, of which 51 are currently operational. CARSNET uses the similar algorithm as AERONET (Dubovik et al., 2000; Dubovik and King, 2000) and has a rigorous calibration process; therefore, the aerosol retrievals of CARSNET are of great importance for determining the temporal and spatial variations of aerosol optical properties in China (Che et al.,

140 2018; Yu et al., 2015; Zhao et al., 2021b; Zheng et al., 2021).

The master instrument used in AERONET and CARSNET is the CE318 Sun photometer, which performs direct Sun and diffuse-sky radiation measurements according to set observation times. For the direct Sun measurements, the radiation is measured at 340, 380, 440, 500, 675, 870, 1020, and 1640 nm to calculate an accurate AOD and at 936 nm for water vapor

145 (WV), with uncertainties within ±0.02 and ±0.10 cm, respectively. The diffuse-sky measurements are conducted at 440, 500,

670, 870, 1020 and 1640 nm to retrieve the microphysical and optical properties of aerosols in different routines: the almucantar (ALM) and the principal plane (PPL). The azimuth angle is varied while the zenith angle is kept constant for the ALM, and vice versa for the PPL. In this study, the CE318s and CW193 were set to perform intensive direct Sun observations every 3 minutes (otherwise every 15 minutes) to obtain enough data to evaluate the AOD accuracy.

2.2.2 CW193 multiwavelength photometer

The CW193 is an automatic photometer and designed to obtain AOD and other retrievals (such as microphysical, optical, and radiative properties of aerosols) from Sun radiation and sky radiation monitoring. The instrument is mainly composed of three parts: optical head, robotic drive platform, and stents system (as shown in the left part of Figure 2). These three parts can be easily connected together only by a few screws. Except for its highly integrated design, the cross weight of CW193 is about 12 kg, and this make it easier to transport. Specifically, we presented the comparison of technical specifications between CE318-T and CW193 in table 1.

Table 1. Technical specifications for CE318-T* and CW193

*Photometer for CE318-T mode in standard version

	CE318-T*	CW193
Main components	Optical head, Control unit, Robot,	Optical head, Robotic drive platform, Stents system
Spectral range	340, 380, 440, 500, 675, 870, 937,1020, 1640 nm	340, 380, 440, 500, 675, 870, 937,1020, 1640 nm
Field of view	1.26°	1.30°
Detection's azimuth range	0° to 360°	0° to 360°
Detection's zenith range	0° to 180°	0° to 180°
Sun tracking accuracy	0.01°	0.02°
Communication outputs	RS232, USB, UMTS/3G/W-CDMA, GPRS	RS232, USB, 4G
Storage	Flash memory (4 MB), SD card (32 G)	Flash memory (32 GB)
Power demand	DC 12 V or Solar panel (5 W) and External batteries (12 V, 16Ah)	DC 12 V
Software	PhotoGetData	DataMonitor

The two collimators within a 1.30° full field-of-view are both screwed tightly to the optical head separately, making its disassembly and maintenance more convenient, to avoid the interference of stray light and reduce the measurement error

originating from the non-parallel integrated collimators used in CE318. To compare the results with AEROENT, the detector in the optical head is designed to equip nine optical filters with nominal wavelengths centered at 340, 380, 440, 500, 675, 870, 936, 1020, and 1640 nm, which are precisely coated to delay the aging of their optical transmittance. There are sensors inside the optical head for internal humidity and temperature monitoring, and this environmental information is used to conduct the temperature correction of the raw signal, minimizing the temperature dependence of the silicon detectors for 1020 nm and 1640 nm.

The robotic drive platform is the main dynamic system to make the optical head track the direct solar radiation, as well as in the ALM scan routines. To avoid mechanical problems owing to excessive usage of robotic platform, the CW193 is designed to keep tracking the Sun all the time, unless the ALM routines are activated at specific integral local time (9:00, 10:00, 11:00, 12.00…). In addition, all the measurements routines will be suspended when the precipitation is detected by the wet sensor of platform, and then the optical head will turn down to avoid the rain contamination. On the whole, protection degrees of these two frames up to IP65, making its tough enough for the running under the humid or dusty environment.

The stents system, directly supported on the base of the robotic drive platform, consists of an adjustable-length tripod with a horizontal adjustment knob at each foot; therefore, it can be quickly deployed and fixed on flat and/or rigid surfaces and has a reliable anti-wind capacity (<25 m s^{-1} if not fixed on the ground). The instrument is powered by a 220 V alternating current, and is also equipped with a solar panel for remote locations and in case of temporary/moveable observation campaigns. As a result, the design of CW193 is very robust, ensuring long-term steady operation in a wide range of temperature and humidity, between about −30°C and 60°C and between about 0 and 100%, respectively.
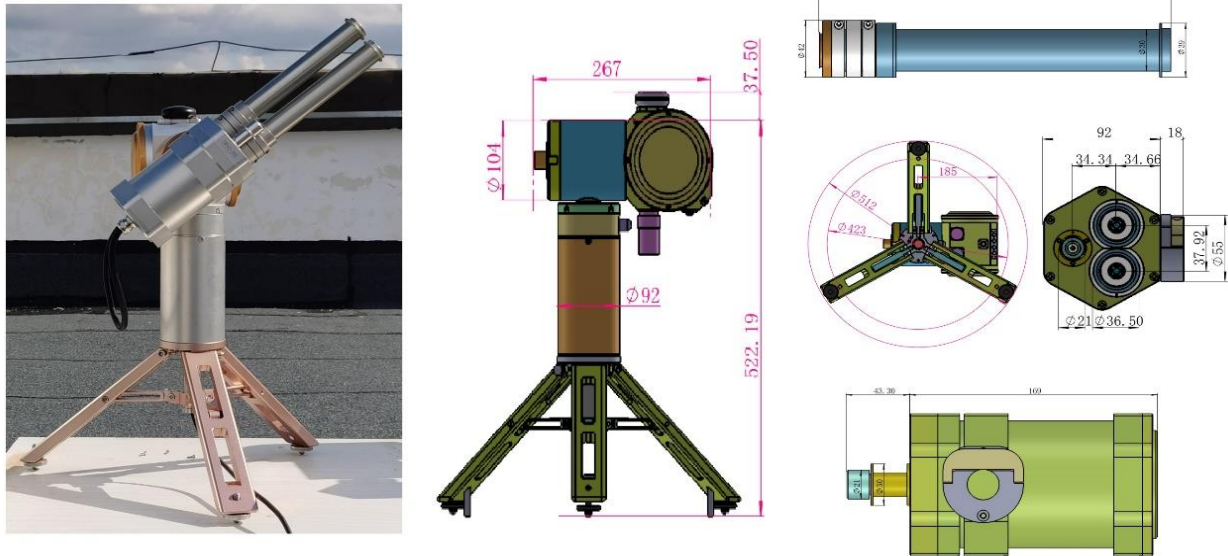
Figure 2. CW193 scheme and dimensions.

185

The main circuit board is in the head of the robotic drive platform, with the integration of operation control, data acquisition, data storage, transmission communication, and status diagnosis. The control unit is designed to conduct observations automatically under the default state, once the geographic information of the observation site is confirmed by the built-in BDS (BeiDou Navigation Satellite System) module. The data unit comprises an internal data logger and a 32 GB memory,
190 considered as life-time storage with a daily data size of ~150 KB. Data transmission to a computer can be realized in two ways: serial communication via RS-232 or the 4G network. The diagnostic module checks the whole system when the instrument is powered on, and the running state can be easily recognized by the indicator light in the optical head.

The system provides a friendly user interface on a computer, which makes the CW193 easy to operate, convenient to maintain,
195 and highly functional. As shown in Figure 3, the functional area and monitoring area are clearly presented in the left and right part of the interface, respectively. It is very convenient to receiving data via 4G network when the serial communication is unavailable in some remote regions, and also in this mode, multiple device control is achievable (device 003, 005 and 006 are on-line and controllable in Figure 3). In data download part, the history data can be easy download by selecting the start and end time via drop-down menu. In the control commands area, all the observation instructions are provided and could be sent
200 to device in the dialog box. In the monitoring area in right half, the plot and its specific data are located in the top and bottom windows, respectively, making it convenient for monitoring the device's status. In summary, we presented the comparison of functional specifications between CE318-T and CW193 in table 2.
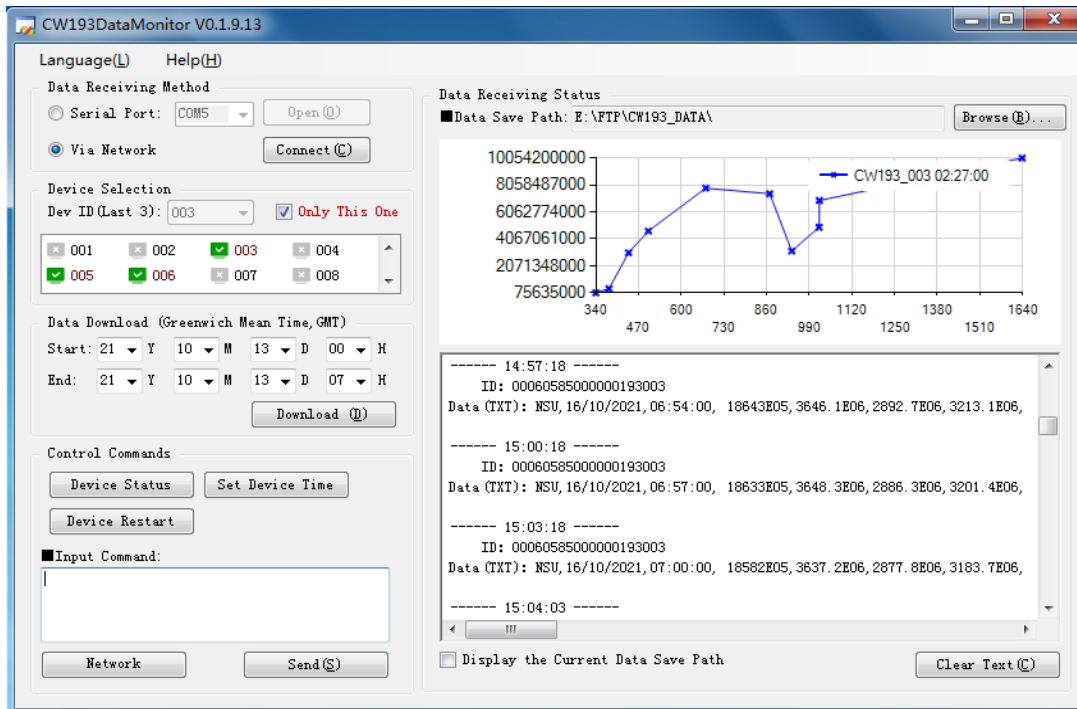
Figure 3. Monitoring software of CW193.

205

Table 2. Functional specifications for CE318-T* and CW193

	CE318-T	CW193
Observation frequency for sun measurement	15 mins (in default), up to 2 mins	3 mins (in default), up to 2 mins
Mode of sun tracking	At the beginning of every measurement	Keep tracking and continuous rotation
Observation frequency for ALM scan	According to air mass, when air mass =1.7, 2.0, 2.2, 2.4, 2.6...	Every integral local time at 7, 8, 9,10, 11...19 O'clock (primary) According to air mass, when air mass =1.7, 2.0, 2.2, 2.4, 2.6... (subsidiary)
Observation schedule**	Sun, Moon, Black, Principal plane, Almucantar, Hybrid, Cross Sun, Cross Moon. Curvature Cross	- Sun, Black, Almucantar, Principal plane (in default) - only Sun (optional, consecutive)

		- only Almucantar (optional, consecutive)
		- only Principal plane (optional, consecutive)
Monitoring Software	- instruments setup - wavelengths selection - scan modes & scenarios configuration - measurement scheduling - data analysis - data visualization - data storage (raw data, k8, ASCII files)	- scan modes & scenarios configuration - measurement scheduling - wavelengths selection - data visualization - data retrieval - data storage (TXT files) - commands inputs - multidevice control (4G mode only)

*Photometer for CE318-T mode in standard version

**Photometer in auto mode

210

2.2.3 Calibration and **data processing**

In this work, the direct Sun calibration of CW193 was conducted at the atmospheric composition observation platform of CAMS (one of the calibration centers of CARSNET), using the method of coefficient transfer (inter-comparison) with the reference master instruments of AERONET (Che et al., 2009, 2019c; Zheng et al., 2021). The sphere calibration was performed

215 at the optical calibration laboratory (CAMS, Beijing) of CARSNET by integrating the sphere. We conducted 50 measurements of the sphere's radiance and found extremely small fluctuations in the CW193 digital counts (<1‰), indicating excellent detection stability and accurate sphere calibration coefficients (Tao et al., 2014).

We calculated the cloud-screened AOD and columnar water vapor of CW193 via the similar algorithm as AERONET. As the

220 algorithm has been used multiple times in many observation campaigns, numerical modelling, and satellite verification for CARSNET, it is suitable and reliable to evaluate the AOD performance of CW193 using this method (Wang et al., 2010; Xia et al., 2021; Yu et al., 2015; Zhao et al., 2021c; Zheng et al., 2021). The algorithm verification is provided in the Supplementary Information to guarantee the accuracy in this campaign (Figures S1 and S2). As for the inversions of VSD and SSA in this campaign, they were retrieved from the observational data from the diffuse-sky measurements of the CW193 at 440, 670, 870,

225 and 1020 nm using the algorithms of Dubovik et al. (2002, 2006). The ADRF was calculated by the radiative transfer module, which is similar to the inversion of AERONET (García et al., 2008, 2012). Because the introduction, validation and application of these inversions and their algorithms have been presented in many previous studies based on CARSNENT observation, we

did not repeat these again in this paper (Che et al., 2018, 2019c; Zhao et al., 2018; Zheng et al., 2021). In general, the AODs' uncertainty was 0.01 to 0.02 (Eck et al., 1999). The VSD accuracy was 15 % to 25 % between 0.1 µm $\leq$ r $\leq$ 7.0 µm while 25 % to 100 % for other radius (Dubovik et al., 2002). The SSA accuracy was 0.03 when its was calculated under the condition of $AOD_{440\ nm}$ >0.50 with a solar zenith angle >50 ° (Dubovik et al., 2002). The bias for measured radiation at the surface was about 9±12 W m^{-2}, affected by the dominant aerosol type (García et al., 2008).

3 Results and discussion

In this work, synchronous measurements with five instruments were conducted at the CAMS observation platform during 1 to 11 November, 2020. Specifically, photometers #543 and #746 of the CE318-N mode and photometers #1043 and #1046 of the CE318-T mode are the four master instruments for the "Beijing-CAMS" site in AERONET, the raw data of which are transmitted in real time to AERONET. The AODs and other inversion products from these four instruments can be downloaded from the AERONET website. Furthermore, these four instruments are also the reference instruments of CARSNET, and have an important role in the operational observations and annual calibration of CARSNET.

3.1 Raw digital counts evaluation

The raw digital counts are the deciding factor for the precision of the calculation and retrieval results, reflecting the running status and stability of the instrument. In Table 3, we show the observed signal with the least squares method, presenting a basic statistical intercomparison at the coincident spectral wavelengths. It is noted that these instruments measure three times within ~30 seconds in one scenario, and we calculated the average values of the digital counts for each observation in this comparison. Furthermore, the results from the AERONET webpage during this campaign were mainly derived from photometers #1043 and #1046 according to the "Instrument Number" in the downloaded files; therefore, we used the corresponding observation signals of these two master instruments to carry out the performance evaluation of CW193. In addition, to avoid the effect of instantaneous atmospheric disturbance, only the values of which the observation time's difference within 20 s compared to the master instruments, were selected and considered as effective data in this work.

From Table 3, it can be seen that the digital counts measured by CW193 and the master instruments are highly correlated for these specific bands, with correlation coefficients (R) and coefficients of determination (R^2) higher than 0.98 and 0.97, respectively, suggesting high linear consistency rather than possible nonlinearities of CW193 in the selected measurement range. For further comparison, we exacted these statistics to four decimal places. It is found that the raw signal from CW193 was generally more consistent with photometer #1046, with all the R^2 values exceeding 0.9988, whereas the R^2 values for photometer #1043 varied from ~0.9792 to 0.9994. In practical terms, the CW193 performs better in the ultraviolet (UV) bands (340 nm and 380 nm) and visible bands (440 nm to 870 nm), with R^2 values larger than 0.9971 and 0.0.9985 with photometers #1043 and #1046, respectively. The R^2 values were relatively low in the infrared bands of 1020 nm and 1640 nm. The minimum

R^2 values were ~0.9792 with photometer #1043 at 1020 nm and ~0.9988 with photometer #1046 at 1640 nm, indicating a greater variation in these two bands than in the other bands owing to its temperature sensitivity (Che et al., 2011; Tao et al., 2014). For the WV channel at 936 nm, the R^2 values were ~0.9977 and ~0.9997 for photometers #1043 and #1046, respectively; hence, the CW193 showed good detection ability for columnar WV.

Table 3. Coefficient of determination (R^2) and number of coincident data (N) for the raw digital counts comparison between CW193 and CE318 measurements for the nine spectral bands used in this study.

Wavelength	#1043			#1046		
(nm)	R	R^2	N	R	R^2	N
340	0.9997	0.9994	162	0.9998	0.9996	355
380	0.9995	0.9990	162	0.9998	0.9996	355
440	0.9997	0.9994	162	0.9998	0.9997	355
500	0.9991	0.9982	162	0.9997	0.9995	355
675	0.9993	0.9985	162	0.9999	0.9998	355
870	0.9985	0.9971	162	0.9999	0.9998	355
936	0.9989	0.9977	162	0.9998	0.9997	355
1020	0.9895	0.9792	162	0.9995	0.9990	355
1640	0.9923	0.9846	162	0.9994	0.9988	355

To obtain a better description of the stability of the instrument and atmospheric conditions, a triplet value is a more effective parameter, which is defined as (maximum − minimum)/mean × 100%. Thus, we calculated the triplets for each band and present its diurnal variation in Figure 4. It can be clearly seen that the triplets show a typical diurnal distribution in this study, as found in many previous studies (Barreto et al., 2016; Che et al., 2011; Estellés et al., 2012), characterized by increasing dispersion with increasing airmass. However, cloud contamination is also an important factor affecting the triplets variation. Using the weather record and the cloud-screening results of AERONET as a reference (Version 3.0), we found that the atmospheric conditions on 7 and 11 November were greatly influenced by cloud processes. As a result, the dispersion of the triplets on these two days was larger than that on the other days, with almost all values exceeding 2.0% at all times. The observation conditions on the other days were less affected by cloud, and it can be seen that the values reduced to a relatively low level, with most values <2.0% between 10:00 and 14:00 BJT (Beijing local time) for all cases. The triplets of the UV bands are as large as 10.0%, whereas they are 2.0−6.0% for the visible bands before 10:00 BJT and after 14:00 BJT. These results reveal that the digital counts of CW193 measurements fluctuate considerably during the morning and the afternoon, owing to the weak solar radiation and rapid and extensive changes of the solar altitudinal angle.
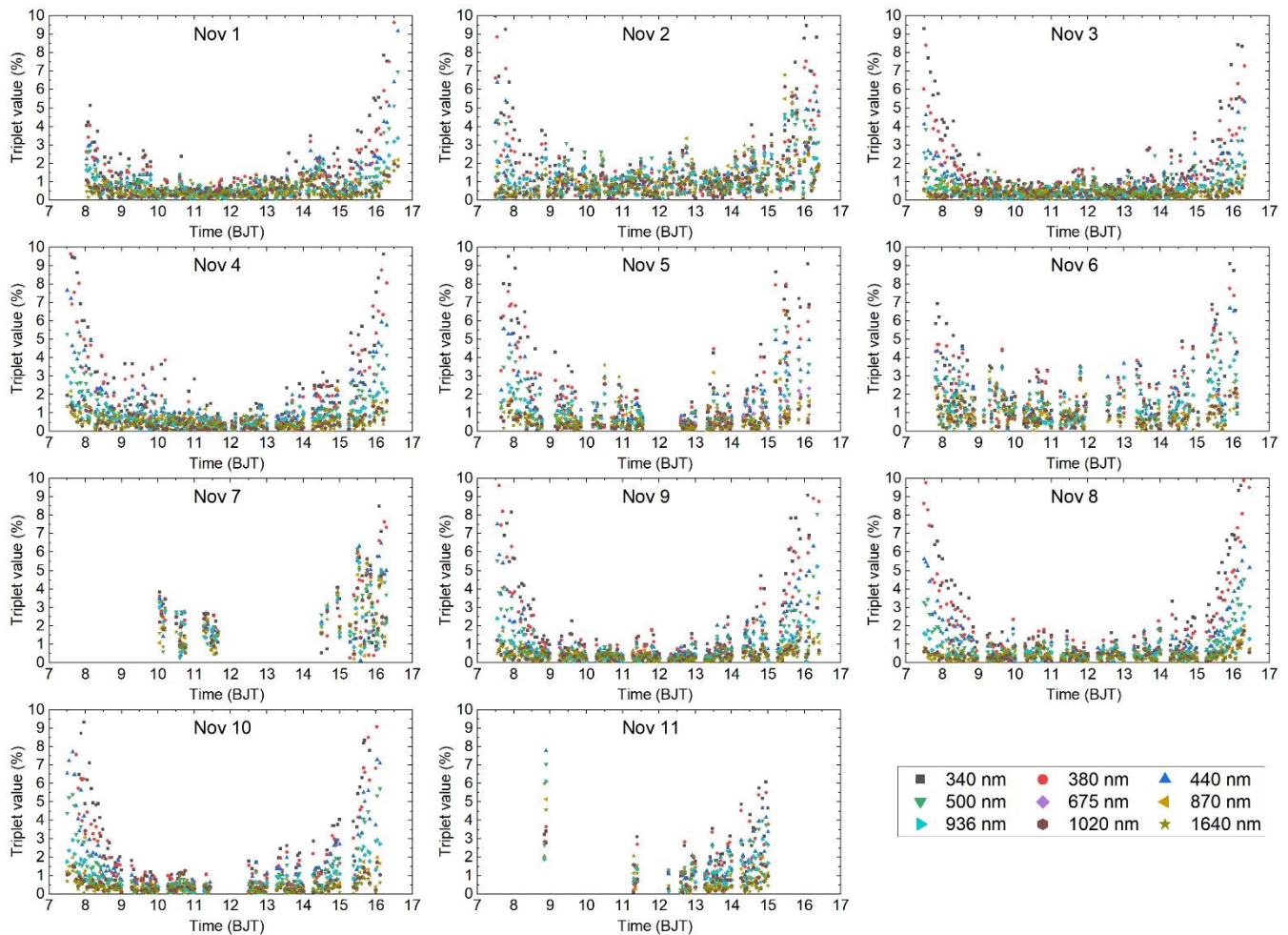
Figure 4. Diurnal variation of triplets at each wavelength on 11 case days.

285

The daily average triplets were also calculated in this intercomparison (Figure 5). We found that the daily average triplets for the UV bands showed the largest fluctuation amplitude range, which were ~1.5−3.0% for 340 nm and 1.2−2.5% for 380 nm. For the visible bands from 440 nm to 870 nm, it can be clearly seen that the variation trend of daily average triplets decreases with increasing wavelength. With the exception of 7 November, which was greatly affected by cloud processes, the daily

290 average triplets in the visible bands were all less than 2.0%. Relatively weak fluctuation amplitudes were observed in the infrared bands from 1020 nm to 1640 nm in all cases, with daily average triplets mostly lower than 1.0%, except on 7 November, and showing less variation with wavelength. The fluctuation for the WV channel at 936 nm was moderate compared with the other bands, and the daily average triplets were slightly higher than those in the infrared bands from 1020 nm to 1640 nm, but much lower than the UV band. In general, the WV had a similar variation range to the 870 nm band, which was ~0.5−2.5%.

295 As can be seen from Figure 5, the lowest daily fluctuations were found on 3 November, with a variation range of ~1.4−1.8% for the UV bands and ~0.4−0.8% for the other bands. Using the meteorological and environmental records as a reference (no cloud contamination and daily $PM_{2.5}$ ~11 μm m^{-3}; Table 4), these results indicate that the dispersion of diurnal triplets is quite small under clear and stable weather conditions, suggesting the reliable measurement capability of CW193.
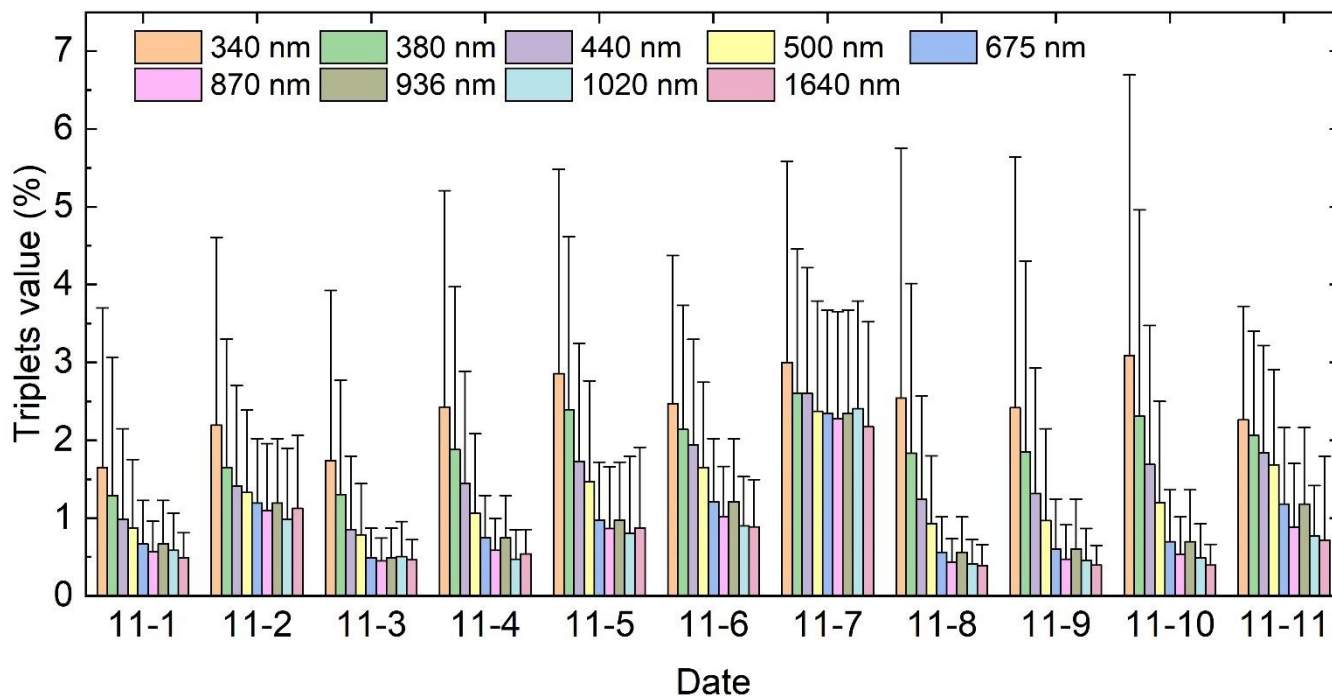
300 **Figure 5. Daily values of triplets at each wavelength on 11 case days.**

3.2 AOD evaluation

The AOD performance of the CW193 was tested at the Beijing-CAMS site, using CE318s as the reference, as the instrument has been widely verified under a wide tange of conditions (Che et al., 2015, 2018; Holben et al., 2001; Xia et al., 2016).

305

First, we examined the wavelength dependance of AOD from CW193, which is an important indicator of the observation precision. Furthermore, the daily average $PM_{2.5}$ and PM_{10} concentrations were calculated for the air quality classification with the reference of the ambient air quality standards of China (GB3095-2012, http://www.mee.gov.cn/gkml/hbb/bwj/201203/t20120302_224147.htm), to achieve a comprehensive evaluation of AOD 310 performance under different atmospheric pollutant loadings. In this study, Level I air quality is defined as daily average $PM_{2.5}$ lower than 35 μg m^{-3}, which indicates that the air quality is quite clean and satisfactory for outdoor activities. Level II reflects

acceptable air quality coincident with a low burden of certain air pollutants, and a daily average $PM_{2.5}$ concentration between 35 μg m^{-3} and 75 μg m^{-3}. Level III indicates mild atmospheric pollution with a daily mean $PM_{2.5}$ concentration of 75−115 μg m^{-3}, under which the time spent on outdoor activities should be reduced for children, older people, and patients.

315

The daily average $PM_{2.5}$ and PM_{10} and the variation range of AOD at 440 nm (AOD_{440}) under the different air quality levels are shown in Table 4. Figure 6 shows the diurnal variation of cloud-screened AOD (only from daytime observation) for each band from CW193 during this campaign. An obvious decreasing trend in AOD with increasing wavelength can be seen, which is in agreement with many previous studies (Che et al., 2019c; Holben et al., 1998; Liang et al., 2019). Consequently, under

320 weak pollution conditions, the high AOD made the characteristics of the wavelength dependance more apparent. On the most polluted day (Level III, $PM_{2.5}$ ~104 μg m^{-3}, AOD_{440} ~1.32−1.47, 11 November), the diurnal AOD was distributed in an orderly pattern and had a similar variation trend at each wavelength, with each curve clearly visible and not intersecting with others. This distribution was also found under the Level II situation on 4 and 10 November. Although AOD_{440} (~0.20−0.60) was relatively smaller than that at Level III, the diurnal AOD curves for each wavelength were more continuous and can be

325 recognized more easily, which is partly attributed to the reduced impact of cloud contamination. In terms of AOD evaluation, the key point is that the performance under quite low aerosol loading is largely affected by the instrument accuracy and stability (Campanelli et al., 2007; Che et al., 2009; Kazadzis et al., 2018; Ningombam et al., 2019; Tao et al., 2014). From Figure 4, it can be seen that, with the exception of 7 November when severe cloud contamination occurred, the variation of AOD curves can be easily identified owing to its wavelength dependence. Under the cleanest conditions (Level I, $PM_{2.5}$ ~6 μg m^{-3}, AOD_{440}

330 ~0.08−0.15, 11 November), despite the cloud contamination in the afternoon, the AOD variation of each band consistently showed a gradually increasing trend, strictly following the rule of decreasing AOD with increasing wavelength. Therefore, in summary, the CW193 showed good ability of AOD's wavelength dependence under both high and low aerosol loadings; hence, the excellent detection ability makes it a reliable instrument for aerosol monitoring.

335

Table 4. Classification of case days based on daily average $PM_{2.5}$ and PM_{10} concentrations and the variation range of AOD_{440}

	Date	$PM_{2.5}$	PM_{10}	AOD_{440}
Level I	11-2	6	42	0.08-0.15
	11-3	11	44	0.09-0.26
	11-8	12	45	0.11-0.21
	11-1	15	73	0.14-0.29
	11-9	23	57	0.14-0.31
	11-7	30	142	0.26-0.47
Level II	11-4	37	77	0.35-0.58
	11-10	43	81	0.20-0.60
Level III	11-5	82	125	0.49-0.91
	11-6	84	147	0.37-0.63
	11-11	104	148	1.32-1.47
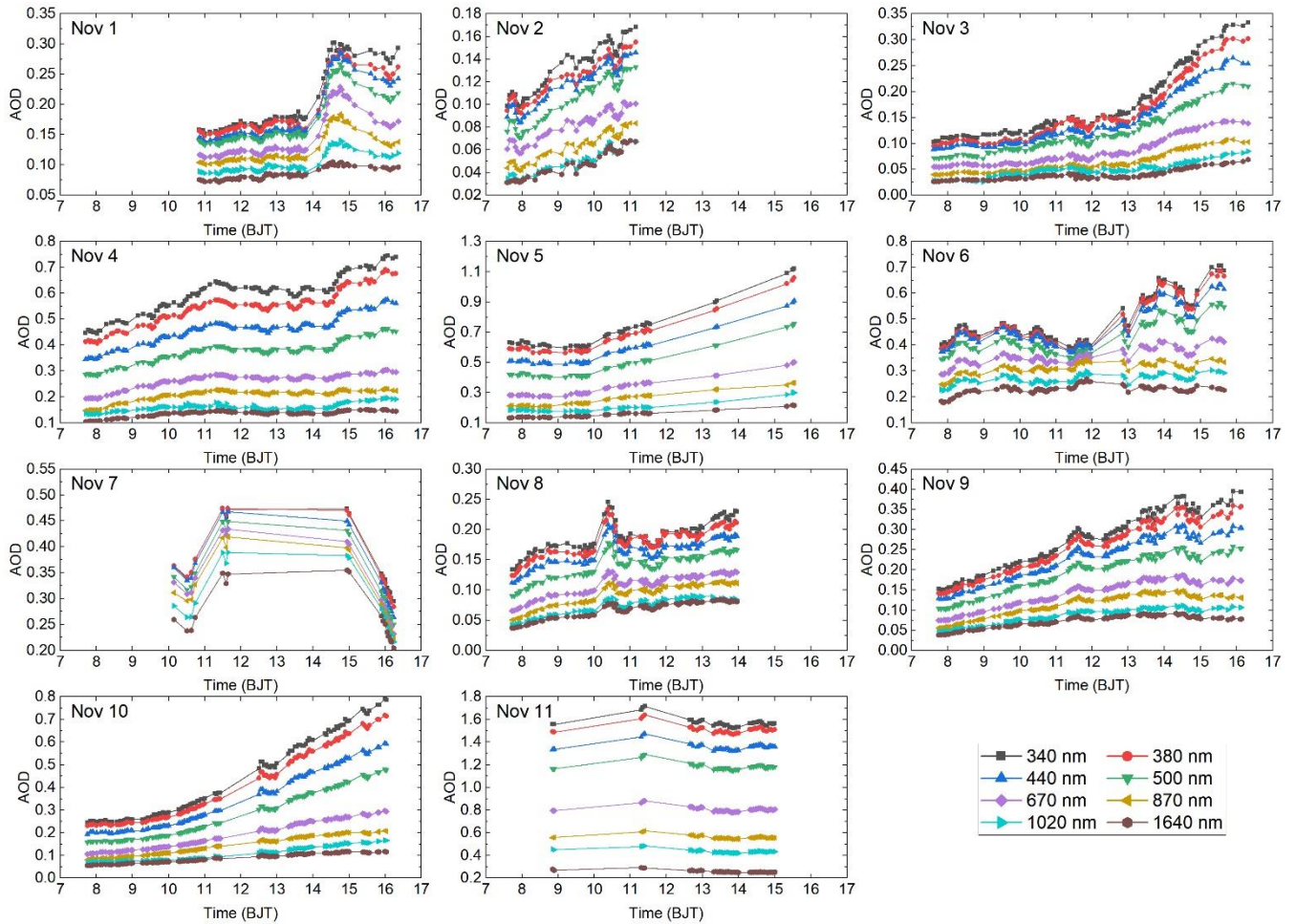
Figure 6. Diurnal variation of AODs at each wavelength on 11 case days.

In the next step, the precision performance of CW193 was validated in detail using the AOD from AERONET as a reference. Figure 7 shows a comparison of the AODs from CW193 with the AODs from AERONET at coincident spectral wavelengths. In general, the AODs from CW193 agree well with AERONET results, with correlation coefficients (R) of ~1.000 for 340−675 nm, ~0.999 for 870 nm, and ~0.997 for 1020 nm and 1640 nm, which indicates that the AODs from CW193 were similarly distributed on both sides of $y = x$ line. From the R values, we can see that the correlation tends to slightly decrease with increasing wavelength. This result can be explained by the temperature sensitivity of the instrument to some degree. As reported by Campanelli et al (2007), the AOD in the near-infrared bands is susceptible to the ambient temperature, and the retrieval accuracy could be improved if the data for the 870 nm and 1020 nm wavelengths were corrected for temperature effects. In addition, although the CW193 is equipped with the same type of temperature sensor in the optical head, there are

still many factors that influence the temperature readings, such as mechanical structure and coating color, which could be the main reasons for the temperature uncertainty and the larger AOD deviation at the longer wavelengths of 870, 1020 and 1640 nm.

From this linear regression figure, it can be seen that the slopes for the 340 nm and 1020 nm bands are ~0.993 and 0.966, respectively, whereas those for the other bands were all larger than 1, varying from ~1.001 to 1.021. This indicates that the AOD from CW193 tends to be higher than that from AERONET. As in many previous AOD validation studies, expected error (EE) analyses were also conducted in this study. We set the envelopes as $\pm(0.05 + 10\%)$. It was found that the AODs from CW193 for each band were all able to achieve a satisfactory performance with 100% retrievals within the EE, much higher than the standard deviation of ~70% (Che et al., 2019b; Levy et al., 2010). The root mean square errors (RMSEs) were all less than 0.05 for all bands, which revealed that the AODs from CW193 are all highly concentrated in the reference AOD range. In addition, these extremely small deviations could also highlight the stability and accuracy of CW193. To evaluate the AOD accuracy further, the relative mean bias (RMB) for each linear regression equation was calculated. As mentioned above, the AOD uncertainties for the near-infrared bands are obviously larger than those for the other bands in this campaign. Specifically, the AODs in the 1020 nm band were underestimated by ~7.8% (RMB = 0.922), whereas they were overestimated by ~11.2% (RMB = 1.112) in the 1640 nm band. The AODs from CW193 in the other bands were all slightly overestimated (~1.6%−4.4%) with the RMB varying in a relatively narrow range of ~1.016−1.044. This indicates that, from the perspective of stability and accuracy, the AODs derived from CW193 have a better performance in the UV bands (340 nm and 380 nm) and visible bands (440 nm to 870 nm) than in the near-infrared band from 1020 nm to 1640 nm. Further studies and experiments still need to be conducted in the future, aimed at algorithm and mechanical structure optimization, to improve the retrieval accuracy.
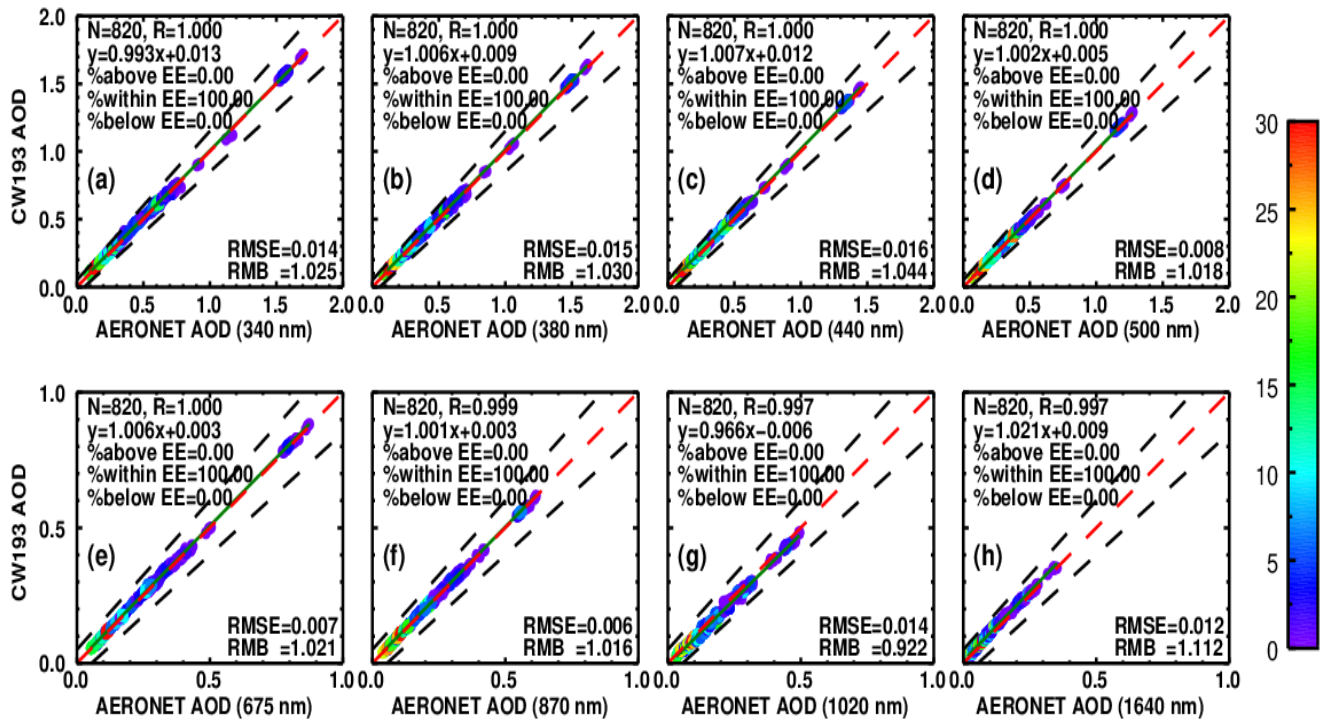
Figure 7. Validation of CW193 AOD at each wavelength against AERONET AOD. One–one line, linear regression line, and the EE envelopes of ± (0.05 + 10%) are plotted as red dashed, green solid, and black dashed lines, respectively.

Figure 8 shows the CW193 AOD bias compared with the equal frequency bins of AOD from AERONET. All collocations of AODs were sorted in ascending order, and then sampled with 20 bins. From the bias boxplots, it can be seen that the mean biases (red dots) have similar trends in the 340 nm to 870 nm bands with a narrow range from about −0.02 to 0.03, characterized by an initial increase, followed by a decrease, and then a slight increase at high AOD. This indicates that the AODs in these bands from CW193 are overestimated at low AOD (for example, AOD_{440} ~0.10 to 0.40). Then under moderate AOD levels (for example, AOD_{440} ~0.50 to 0.90), these biases become smaller or almost equal to zero (even little bit negative) in the range of about −0.01 to 0.01, indicating that the calculations were more consistent with reference values and a high accuracy. At high AOD levels (for example, AOD_{440} ~1.30 to 1.50), a slight increase in bias was observed in this campaign, with mean values varying from about 0 to 0.02. However, the bias performance for the 1020 nm and 1640 nm bands were quite different. For the 1020 nm band, the mean biases decreased from zero to −0.02, consistent with AOD varying from ~0.05 to 0.20, and remained relatively constant at about −0.02 when the AOD continually increased to ~0.50. For the biases at 1640 nm, the mean values of each bin showed a roughly parabolic distribution varying from ~0.01 to 0.02, consistent with the AOD varying from ~0.02 to 0.36. Similar to the results mentioned above, the different distribution of the bias boxes for the near-infrared bands

suggests that an improvement in accuracy is in needed. Although the linear regression and bias showed fluctuations to some degree, the AOD performance of CW193 was outstanding with high accuracy and stability based on the comprehensive analysis above, characterized by a bias concentrated within ~0.02 for the visible and near-infrared bands and within ~0.03 for the UV bands, which meets the accuracy requirements for AERONET (Holben et al., 1998).

415
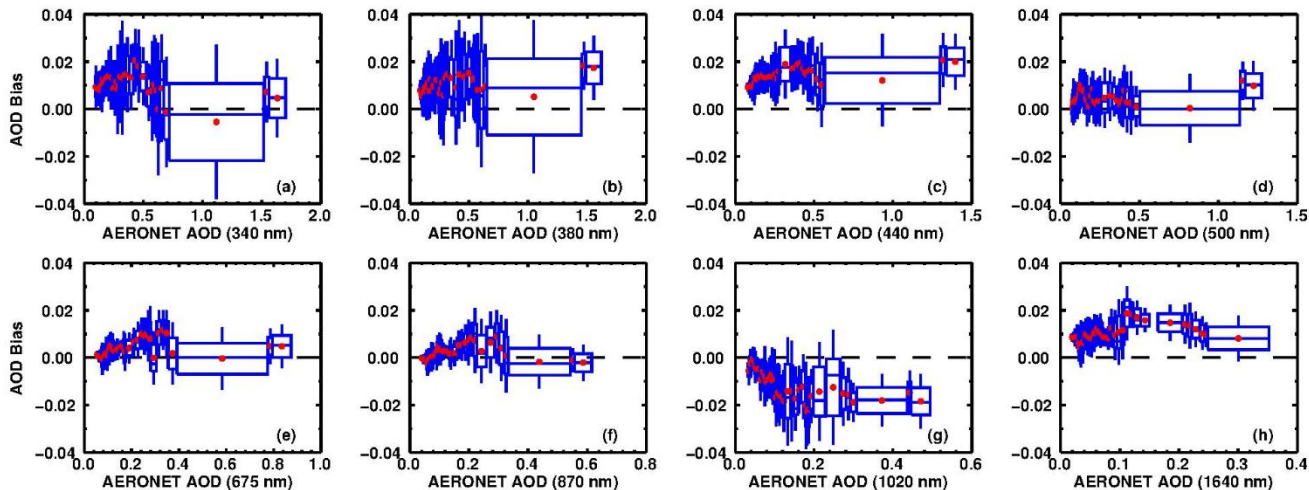
Figure 8. AOD bias boxplots of CW193 AOD and AERONET AOD using 25% and 75% percentiles with 20 bins. The red dashed line is the one–one line and indicates zero bias. The red dot, middle line, and upper and lower hinges represent the mean, median of the AOD bias, and 25% and 75% percentiles, respectively.

420 **3.3 Inversions evaluation**

According to the algorithm, the aerosol inversions, including microphysical, optical, and radiative properties, are retrieved from the aureole and sky radiance measurements. Similar to CE318, the CW193 conducts the ALM routine at a specific time related to airmass, which is performed in two wings in the 440, 675, 870, and 1020 nm bands sequentially: right (azimuth angle displaced towards the right of the Sun position) and left (azimuth angle displaced towards the left of the Sun position).

425 In this study, we chose the VSD, SSA, and ADRF to represent the microphysical, optical, and radiative properties of aerosols, as they are not only widely used parameters in current research but also the most important factors influencing the radiative budget of the Earth–atmosphere system (Wang et al., 2013; Zhang et al., 2018). However, it is noted that the uncertainties of these inversions are more difficult to ascertain. As the aureole and sky radiance measurements constitute only single observations (from one ALM routine) and the observation time of each sequence at a specific wavelength is largely subject to

430 the mechanical design and instrument version (for example, the CE318-T mode has faster robotic movements than the N mode). Furthermore, there is no absolute self-calibration procedure between the sphere calibrations; therefore, the uncertainty in the

sky radiance at the time of calibration is assumed to be <5% for these four channels (Holben et al., 1998). As reported by Tao et al (2014), the sphere calibration results of CARSNET differed by 3.12−5.24% in the 870 nm and 1020 nm bands, whereas is differed within 3% in the other two bands compared with the original values from Cimel. In addition, to avoid disturbance from transient atmospheric processes, only the results with an observation time deviation of less than 10 minutes from those of AERONET were selected and the related inversions of CARSNET were also retrieved and presented to show a more detailed comparison.

3.3.1 Volume size distribution

Figure 9 shows a comparison of the VSD for four selected cases in this campaign. It can be seen that the results from CW193 can accurately present the variation pattern of aerosols: the typical bimodal distribution on 6 and 10 November and the nearly unimodal distribution for the two cases on 7 November. For fine-mode particles (radius <1.00 μm), the variations were apparently observed on 6 and 10 November. For the reference PM concentrations, the ratio of $PM_{2.5}/PM_{10}$ was ~53.1−57.1%, suggesting a certain amount of small particles, which agrees with the distribution pattern from CW193 and AERONET. The maximum volume of fine-mode particles varied in the range of ~0.03−0.05 $μm^3 μm^{-2}$ and ~0.07−0.08 $μm^3 μm^{-2}$ for 6 and 10 November, respectively. Specifically, the largest deviations of the maximum for fine-mode particles occurred on 6 November, ~77.6% and ~57.1% for CW193 and CARSNET compared with AERONET, respectively. Despite the large volume deviations for fine-mode particles, the variation trends were consistent with those of AERONET, characterized by a maximum peak at a radius of 0.15 μm. Hence, these patterns can be attributed to the different observation times to some degree. The time deviation varied from ~3 to 4 minutes compared with AERONET in this case, while the fine-mode volumes showed a gradually decreasing trend from CW193, followed by CARSNET and AERONET, which agreed with the time series. In contrast, the small deviations of the maximum for fine-mode particles occurred on 10 November, ~8.9% and ~6.8% for CW193 and CARSNET compared with AERONET, respectively. The peak of CW193 and AERONET occurred at a radius of 0.11 μm, and the peak of CARSNEET was observed at 0.15 μm, indicating that both CW193 and CARSNET show good consistency with AERONET.

For coarse-mode particles (radius >1.00 μm), the variations were clearly detected for the four cases, especially on 7 November when the ratio of $PM_{2.5}/PM_{10}$ was ~21.1%, suggesting that large aerosols were dominant. In these four cases, the peak volumes of coarse-mode particles varied in the range ~0.09−0.13 $μm^3 μm^{-2}$, ~0.11−0.14 $μm^3 μm^{-2}$, ~0.18−0.25 $μm^3 μm^{-2}$, and ~0.05−0.07 $μm^3 μm^{-2}$, respectively. It can be seen that the high deviations of the peak volume from CW193 were observed for the cases of 6 and 7 November, with values of ~29.2%, ~19.1% (the case around 8 AM), and 22.2% (the case around 12 AM) compared with AERONET, respectively. However, the performance of CARSNET was better than that of CW193 in these three cases, with deviations of ~5.7%, ~20.4%, and ~6.7%, respectively. As mentioned above, except for the calibration and algorithm uncertainties, these large deviations could be explained by the influence of instantaneous atmospheric disturbances on the retrievals, although the time difference of the measurements between CW193 and AERONET were within ~4−8 minutes

465 (~3−4 minutes for CARSNET). A narrow variation range was found for the 10 November case, characterized by a relatively small time difference among these three retrievals (~2−4 minutes). Consequently, the deviation of the peak volume for CW193 was ~13.1% compared with AERONET, while a larger difference of ~16.8% was found for CARSNET. In summary, the difference in the VSD showed an obvious time-correlation regularity—the smaller the deviation with time, the better the retrieval consistency with AERONET.

470
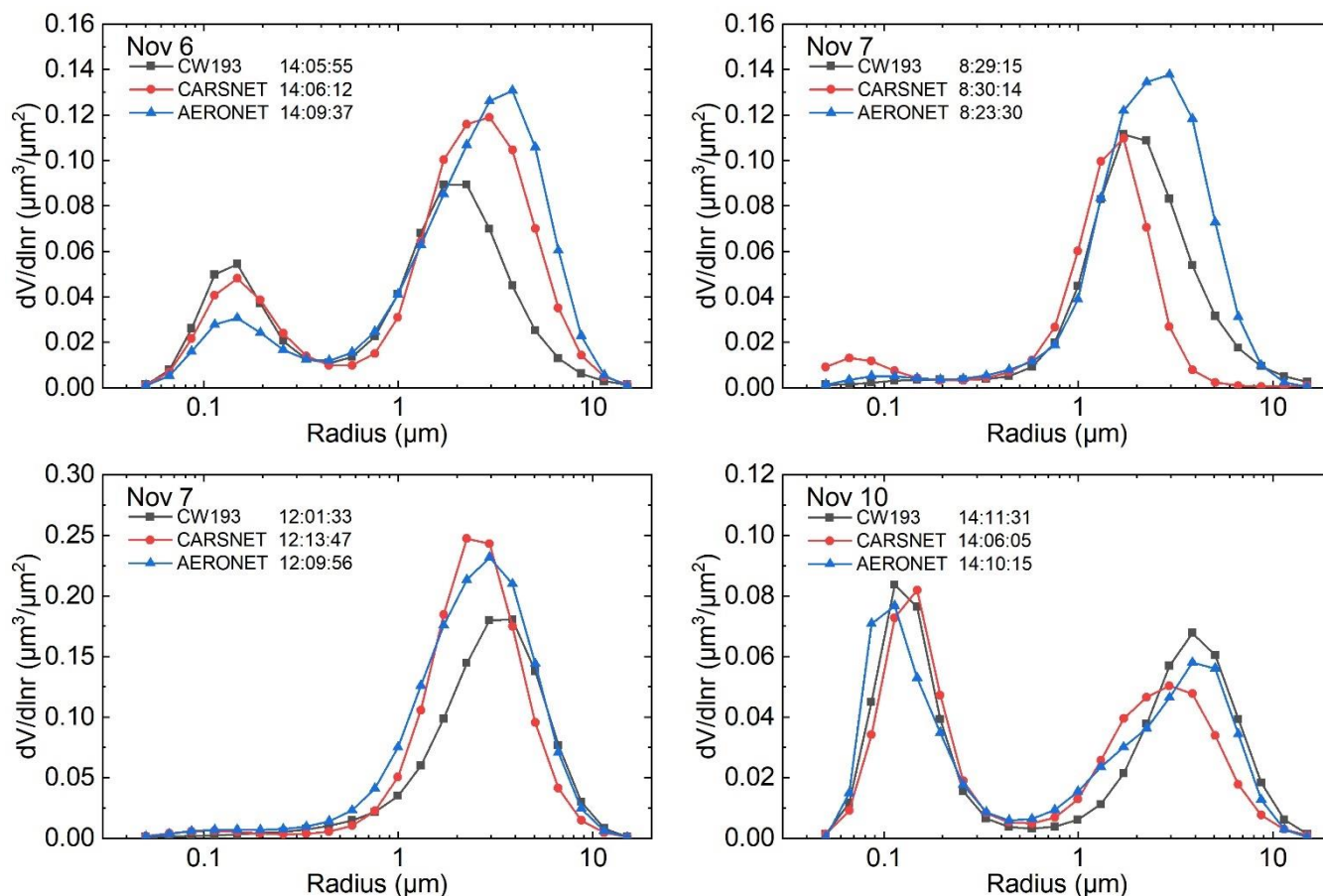
Figure 9. Comparison of retrieved VSD for CW193, CARSNET, and AERONET for four selected cases.

3.3.2 Single scattering albedo

The SSA represents the scattering proportion affected by aerosol particles in the total extinction and is one of the key variables
475 in assessing the effects of aerosols on the climate (Che et al., 2019c; Zhao et al., 2018). The variation of SSA at four spectral wavelengths for the four cases (6 and 10 November and two on 7 November) is shown in Figure 10. First, we examined the wavelength dependence of SSA, revealing the different scattering capacity for aerosols at specific bands, which is largely

influenced by the aerosol chemical composition and can be regarded as an indicator of the dominant aerosol type (Eck et al., 1999; Zheng et al., 2021). It can be seen from Figure 10 that the SSA on the three days showed different variation trends.

480   Specifically, for the 6 November case, the SSA increased from 440 nm to 675 nm and showed a roughly decreasing trend from 675 nm to 1020 nm, indicating a relatively strong aerosol absorbance at shorter wavelengths in the visible bands. The SSA showed an increasing trend with wavelength for the two cases on 7 November, whereas a decreasing trend was observed on 10 November. This indicates that the aerosol absorptive ability was attenuated with increasing wavelength on 7 November, whereas enhanced aerosol absorbance with wavelength was found on 10 November. From the discussion above, we can see

485   that the wavelength dependence of SSA from CW193 and CARSNET were both highly consistent with that from AERONET, indicating the good performance of the retrieval for aerosol optical properties.

To elaborate the SSA assessment, we present a comprehensive comparison of the accuracy in detail here. On 6 November, the SSA peaked in the 675 nm band, with values of ~0.848, 0.857, and 0.853 for CW193, CARSNET, and AERONET, respectively. The deviations of these maximums for CW193 and CARSNET were ~0.1% and 0.3% compared with AERONET, respectively.

490   In this case, the SSA of CW193 varied within a narrow range of ~0.834−0.848, whereas that of AERONET was ~0.836−0.853. The highest deviation for a specific wavelength of CW193 was found in the 1020 nm band, with a value of ~1.7%, and the lowest was found in the 440 nm and 870 nm bands, with a value ~0.1%. As mentioned above, the SSA shows an increasing trend with wavelength for the two cases on 7 November. The smallest SSA values were all observed in the 440 nm bands, with values varying in the range of ~0.858−0.861 and ~0.840−0.859, respectively. For the case at around 08:00, the maximum of

495   CW193 was found in the 870 nm band, with a value of ~0.899, whereas that of AERONET was found in the 1020 nm band, with a value of ~0.911, which suggests a maximum deviation of ~1.3%. The largest deviation for a specific wavelength of CW193 occurred in the 1020 nm band and was ~2.1% compared with AERONET, followed by 1.9% at 675 nm, 1.0% at 870 nm, and 0.6% at 440 nm. For the case at around 12:00, although the SSA was relatively low in the 440 nm band (~0.840−0.859), it remained almost constant from 675 to 1020 nm for CW193 and AERONET, characterized by a small fluctuation amplitude

500   of ~0.930−0.935 for the former and ~0.926−0.931 for the latter. The highest deviation for a specific wavelength, ~1.8%, was measured in the 440 nm band, followed by 0.8% at 1020 nm, 0.6% at 675 nm, and 0.1% at 870 nm. The SSA showed more obvious fluctuations for the 10 November case. Specifically, the peak SSA for CW193 and AERONET were both observed in the 440 nm band, with values of ~0.844 and 0.832, respectively. Likewise, the lowest values of ~0.733 and 0.708 for these two were measured in the 1020 nm band. However, the variation of deviation at a specific wavelength showed no regular pattern

505   compared with the SSA. The largest deviation of ~3.5% was found in the 1020 nm band, followed by ~2.6% at 870 nm, ~1.4% at 440 nm, and ~0.7% at 765 nm. In a conclusion, the SSA deviation between CW193 and AERONET varied in the range of ~0.1−1.8%, ~0.6−1.9%, ~0.1−2.6%, and ~0.8−3.5% for the 440, 675, 870, and 1020 nm bands, respectively, indicating a high consistency with AERONET.
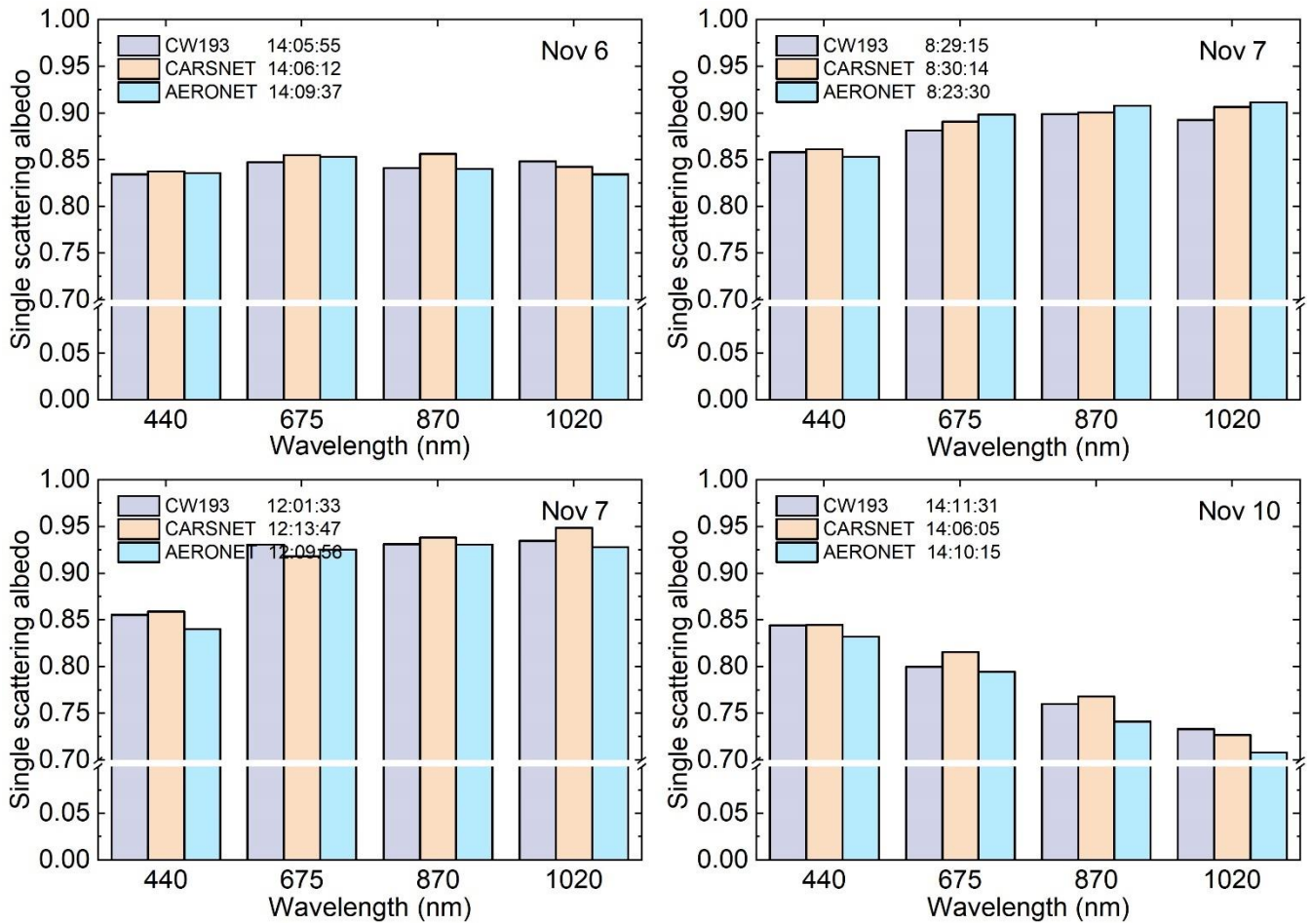
510   **Figure 10. Comparison of retrieved SSA for CW193, CARSNET, and AERONET for four selected cases.**

3.3.3 Aerosol direct radiative forcing

The ADRF is a key factor influencing the radiation budget of the Earth–atmosphere system, in which any small perturbation to this global energy balance can cause a profound change in the climate (García et al., 2012). In this context, much progress

515   had been made in this field to provide insight into the climate effects of aerosols. A previous study estimated the total anthropogenic radiative effect on a global scale to be +1.6 (−1.0 to +0.8) W m^{-2}, of which −0.5 (±0.4) W m^{-2} is associated with the direct radiative forcing of aerosols (García et al., 2008). However, it can be seen that there remains huge uncertainty in the evaluation of the ADFR. For this reason, we selected it as a main product of CW193 to examine the accuracy of the radiative retrieval.

520

In Figure 11, we show a comparison of ADRF for the four cases (6 and 10 November and two on 7 November) between the CW193, CARSNET, and AERONET. As reported by Zheng et al. (2019), the ADRF at Earth's surface (BOA) varies from −86±31 to −132±50 W m^{-2}, whereas the ARDF at the top of the atmosphere (TOA) varies from −35±18 to −55±26 W m^{-2} based on a five-year observation campaign in urban Beijing. Therefore, it can be seen that the BOA and TOA retrievals of CW193 and CARSNET all show a reasonable range of values in this campaign. Specifically, the BOAs of CW193 were −127.1, −65.6, −108.4, and –105.6 W m^{-2} for the four cases in chronological order, respectively. Correspondingly, the BOAs from AERONET were −113.2, −58.4, −103.5, and –95.0 W m^{-2}. Thus, the deviation of BOAs in these cases was ~12.2%, 12.3%, 4.8%, and 11.2%, respectively, suggesting an overestimation of BOA compared with AERONET. For the TOAs, the CW193 retrievals for these cases were −22.8, −25.6 −34.3, and –16.5 W m^{-2}, whereas the reference values from AERONET were −25.3, −22.1, −32.6, and –15.3 W m^{-2}, respectively. That is, the TOA deviation found in these cases was ~9.8%, 15.9%, 5.4%, and 7.4%, respectively. In summary, the deviation of the retrieval BOA was ~5%−12%, whereas it was ~5%−16% for the TOA. As shown above, the relatively larger uncertainties can be partly explained by the inherent algorithm error, as well as the difference in observation time.
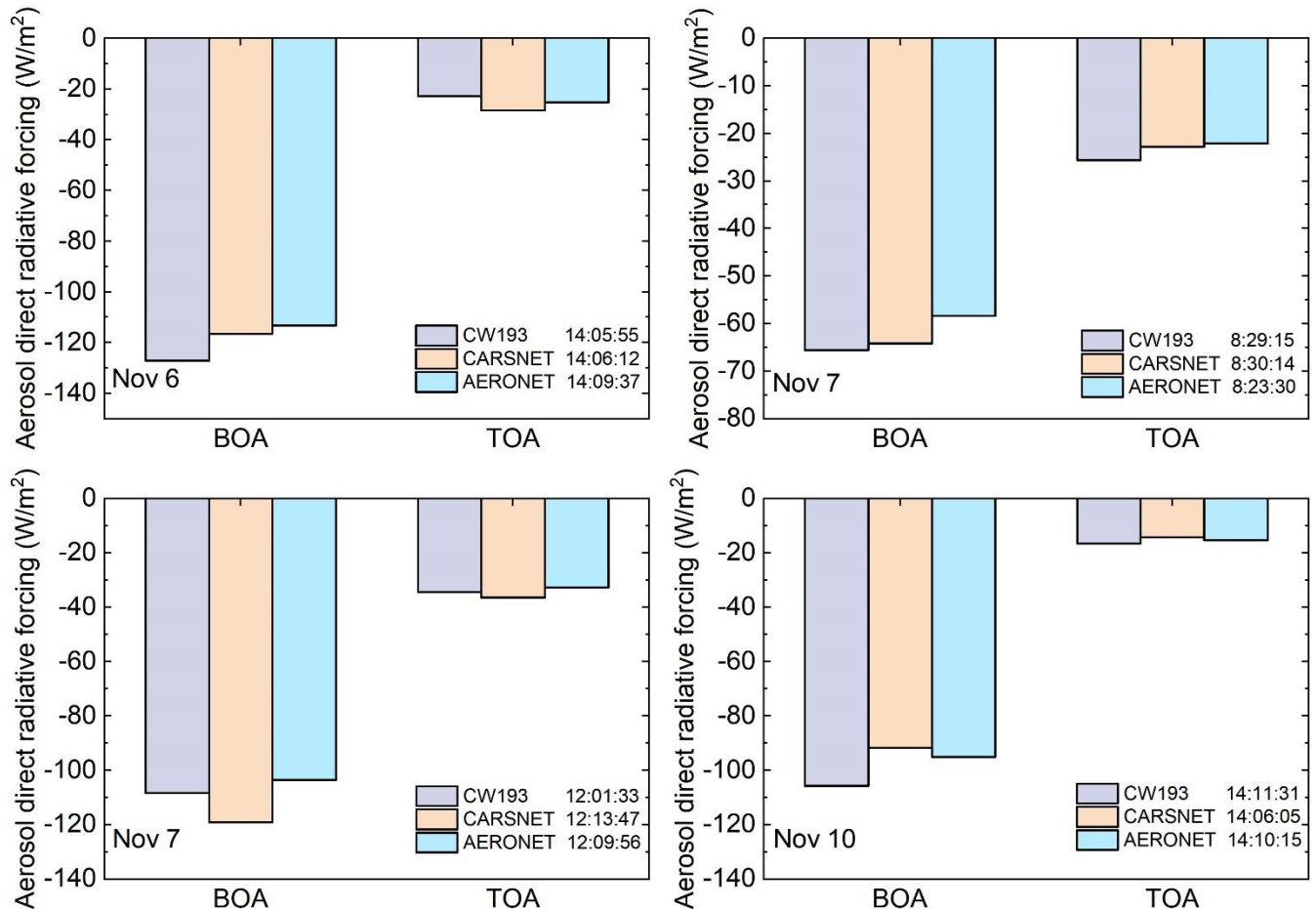
Figure 11. Comparison of retrieved ADRF for CW193, CARSNET, and AERONET for four selected cases.

3.4 Water vapor evaluation

Water vapor (WV) is a key atmospheric component for studies of climate change, because it not only has an important role in aerosol aging but also can influence the energy budget of the Earth–atmosphere system by absorbing and scattering solar energy. Therefore, in this study, the precision performance of WV from CW193 was validated in detail using AERONET as a reference.

Figure 12 shows a comparison of WV from CW193 with the results from AERONET. In Figure 12 (a), it can be seen that the WV from CW193 agrees well with AERONET WV, with a correlation coefficient (R) of ~0.997. From this linear regression, the slope was ~0.941, suggesting that the WV from CW193 tends to be lower than that from AERONET. In terms of RMB values, it is found that the WV from CW193 is underestimated by ~2.1% (RMB = 0.979). The EE analysis showed that the retrieved columnar WV (100%) was within the EE. In addition, the small RMSE (~0.020) also reflected that the CW193 WV was highly concentrated in the reference AERONET range.

Figure 12 (b) shows the CW193 WV bias compared with equal frequency bins of WV from AERONET. From this boxplot, it can be seen that the biases vary in the range of −0.04 to 0.04, whereas its mean values (red dots) are concentrated in a narrower range from −0.02 to 0.02. As reported by Holben et al. (1998), the uncertainty of the WV retrieval is limited to less than 12%, based on an intercomparison with radiosonde results. In this study, the overall WV biases of CW193 was roughly lower than 4%, demonstrating the accurate measurement capability for columnar WV. However, it is noted that these biases, especially the mean values, show an increasing trend (about −0.01 to 0.03) with increasing WV values (~0.24 to 0.80 cm). Gui et al (2017) revealed that the monthly WV for November was ~0.74 cm in urban Beijing, whereas that for the summer exceeded 2.00 cm. In this campaign, the CW193 WV varied from ~0.26 to 1.08, indicating that whether this bias increasing trend exists still needs to be further tested in future, especially for humid summer days.
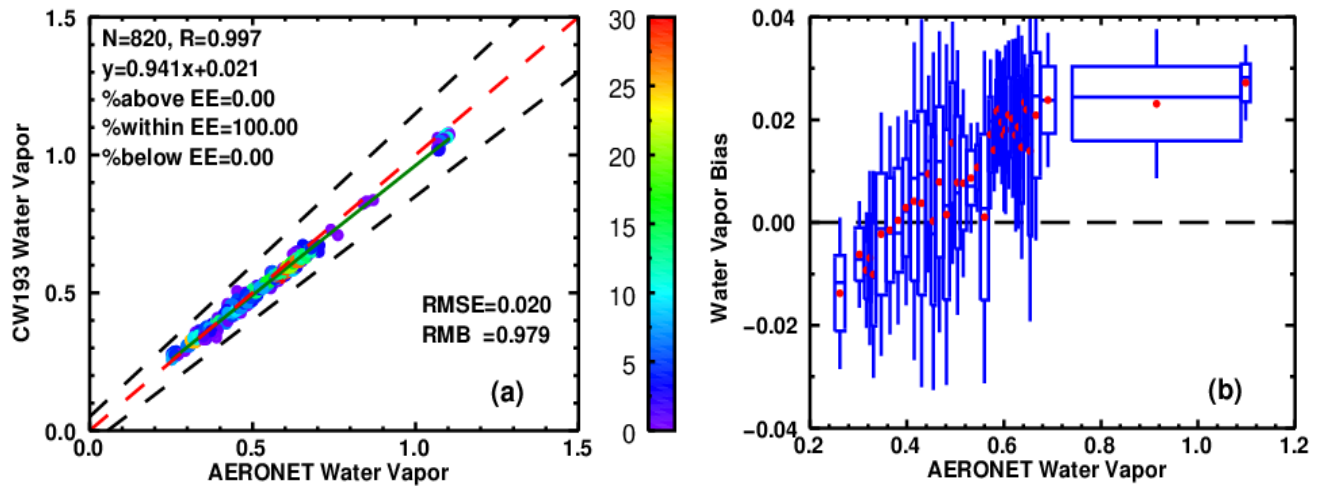
Figure 12. The same as Figure 7 and Figure 8 but for water vapor (unit: cm).

4 Conclusions

In this study, we have presented a multiwavelength photometer named CW193 for monitoring aerosol microphysical, optical, and radiative properties. The CW193 is highly integrated and is composed of three main parts: optical head, robotic drive platform, and stents system. It has a user-friendly interface and all commands can be sent to the instrument via serial communication or the 4G network, which makes data acquisition and operation monitoring easier. A performance evaluation of CW193 was presented and discussed in detail, based on an intercomparison with the reference AERONET results. The main conclusions of this study are as follows.

1. The comparison of raw digital counts from CW193 and CE318s (two AERONET master instruments, photometers #1043 and #1046) showed a high coefficient of determination (R^2) for all wavelengths, which were >0.97 and >0.99, respectively. Apart from the cloud contamination, the diurnal triplets for these 9 bands were mostly lower than 2.0% during 10:00 to 14:00 BJT. Daily average triplets for the UV bands (340 nm and 380 nm) varied from about 1.2% to 3.0%, whereas it was <2.0% for the visible and infrared bands (440 nm to 1640 nm).

2. Using reference PM concentrations, the wavelength dependance of AODs was examined. The AOD curves were non-intersecting and could be easily identified (AOD_{440} ~0.08 to 1.47) under the air quality Level I to Level III ($PM_{2.5}$ ~6 to 104

μg m^{-3})**,** showing a decreasing trend with increasing wavelength. From the regression analysis, a good AOD agreement ($R >$ 0.99) and RMSE values from 0.006 (870 nm) to 0.016 (440 nm) were observed. The AODs from CW193 achieved a satisfactory performance with 100% of the retrievals within the EE (0.05 + 10%) and a RMB varying from 0.922 to 1.112. The AOD bias analysis showed an overall deviation that varied within ±0.04, and within 0.02 for the mean values.

3. The variation of inversions was subject to the time of the measurement in this study. From the perspective of VSD retrievals, the deviations of the maximum for fine-mode particles varied from ~8.9% to 77.6%, whereas it varied from ~13.1% to 29.1% for coarse-mode particles. The wavelength dependance of SSA from CW193 showed a similar trend to the AERONET SSA, and the variation range of the deviations was ~0.1−1.8%, ~0.6−1.9%, ~0.1−2.6%, and ~0.8−3.5% for the 440, 675, 870, and 1020 nm bands, respectively. For the ADRF, the BOA and TOA deviations of ~4.8%−12.3% and ~5.4%−15.9% were observed in this study, respectively.

4. A good WV agreement was found, characterized by a high R (~0.997), small RMSE (~0.020), and satisfactory EE distribution (100% within EE). The RMB showed that the WV was underestimated by ~2.1% (RMB = 0.979). The biases mostly varied within ±0.04 cm, whereas its mean values were concentrated within ±0.02 cm.

The results of this preliminary evaluation indicate that the CW193 is appropriate for monitoring aerosol microphysical, optical, and radiative properties, with the overall AOD (including WV) biases within ±0.02 for the 500 nm to 870 nm bands and within ±0.04 for the other bands. Considering the uncertainty inherent in the algorithm (±0.02) and the AOD uncertainty of AERONET (±0.02), the direct Sun measurements seem reasonable and reliable for the AOD and WV calculations (uncertainty within ±0.04). However, its performance under extreme heavy aerosol loading still needs to be assessed in future, especially during severe haze and/or dust episodes when the AOD exceeds 2.00. Although the results for SSA and ADRF showed good agreement with AERONET, the VSD deviations were relatively larger than these two parameters. In fact, owing to the joint influence of the sphere calibration's uncertainty and the measurement time difference, the evaluation of these inversions was difficult under the short period of the observation campaign. Consequently, the instruments still need to be further tested under different environment conditions, including long-term observations in mountainous, coastal, and desert regions with the reference of CE318, POM-02 and PFR. As a result, the CW193 retrievals in this study showed high precision for SSA and ADRF, and comparable results for VSD, indicating the good comparability and consistency with AERONET.

Above all, the highly integrated design and smart control performance make CW193 suitable for the monitoring microphysical, optical, and radiative properties of aerosol. Due to its smart control performance and optional observation schedule, such as ALM mode, the CW193 could meet the different requirement of the aerosol microphysical, optical, and radiative properties. When the VSD and SSA is in great demand for the modification of numerical model and the verification of satellite inversion products, these inversions could be obtained about 2 to 3 times in an hour, while for once in default observation schedule. As

a result, this instrument could be regarded as a contributor in regional and climate model data assimilation, satellite modification, and improving knowledge of the temporal and spatial variations of aerosols.

Data availability

Datasets used in the present study are available from the corresponding author on reasonable request.

Author contribution

HZC and XYZ designed the research. HZC, YPW, XQH and XCZ built the device. XAX and JZ performed the calculation. JBZ, HJZ and KG analysed the data. YZ and LL wrote the paper. All authors discussed the results and commented on the paper.

Competing interests

The authors declare that they have no conflict of interest.

Financial support

This research has been supported by the National Science Fund for Distinguished Young Scholars (grant no. 41825011), the National Natural Science Foundation of China project (grant no. 42030608, 42105138, 41975161, 41905117, 42175153) and Basic Research Fund of CAMS (grant no. 451336)

References

Barreto, Á., Cuevas, E., Granados-Muñoz, M. J., Alados-Arboledas, L., Romero, P. M., Gröbner, J., Kouremeti, N., Almansa, A. F., Stone, T., Toledano, C., Román, R., Sorokin, M., Holben, B., Canini, M. and Yela, M.: The new sun-sky-lunar Cimel CE318-T multiband photometer – A comprehensive performance evaluation, Atmos. Meas. Tech., 9(2), 631–654, doi:10.5194/AMT-9-631-2016, 2016.

Bi, J., Huang, J., Hu, Z., Holben, B. N. and Guo, Z.: Investigating the aerosol optical and radiative characteristics of heavy haze episodes in Beijing during January of 2013, J. Geophys. Res. Atmos., 119(16), 9884–9900, doi:10.1002/2014JD021757, 2014.

Campanelli, M., Estellés, V., Tomasi, C., Nakajima, T., Malvestuto, V. and Martínez-Lozano, J. A.: Application of the SKYRAD improved Langley plot method for the in situ calibration of CIMEL Sun-sky photometers, Appl. Opt., 46(14), 2688–2702, doi:10.1364/AO.46.002688, 2007.

Charlson, R. J., Schwartz, S. E., Hales, J. M., Cess, R. D., J. A. Coakley, J., Hansen, J. E. and Hofmann, D. J.: Climate Forcing by Anthropogenic Aerosols, Science (80-.)., 255(5043), 423–430, doi:10.1126/SCIENCE.255.5043.423, 1992.

640 Che, H., Zhang, X., Chen, H., Damiri, B., Goloub, P., Li, Z., Zhang, X., Wei, Y., Zhou, H., Dong, F., Li, D. and Zhou, T.: Instrument calibration and aerosol optical depth validation of the China Aerosol Remote Sensing Network, J. Geophys. Res. Atmos., 114(D3), doi:10.1029/2008JD011030, 2009.

Che, H., Wang, Y., Sun, J. and Zhang, X.: Assessment of In-situ Langley Calibration of CE-318 Sunphotometer at Mt. Waliguan Observatory, China, SOLA, 7(1), 89–92, doi:10.2151/SOLA.2011-023, 2011.

645 Che, H., Zhang, X. Y., Xia, X., Goloub, P., Holben, B., Zhao, H., Wang, Y., Zhang, X. C., Wang, H., Blarel, L., Damiri, B., Zhang, R., Deng, X., Ma, Y., Wang, T., Geng, F., Qi, B., Zhu, J., Yu, J., Chen, Q. and Shi, G.: Ground-based aerosol climatology of China: Aerosol optical depths from the China Aerosol Remote Sensing Network (CARSNET) 2002-2013, Atmos. Chem. Phys., 15(13), 7619–7652, doi:10.5194/ACP-15-7619-2015, 2015.

Che, H., Qi, B., Zhao, H., Xia, X., Eck, T. F., Goloub, P., Dubovik, O., Estelles, V., Cuevas-Agulló, E., Blarel, L., Wu, Y., 650 Zhu, J., Du, R., Wang, Y., Wang, H., Gui, K., Yu, J., Zheng, Y., Sun, T., Chen, Q., Shi, G. and Zhang, X.: Aerosol optical properties and direct radiative forcing based on measurements from the China Aerosol Remote Sensing Network (CARSNET) in eastern China, Atmos. Chem. Phys., 18(1), 405–425, doi:10.5194/ACP-18-405-2018, 2018.

Che, H., Gui, K., Xia, X., Wang, Y., Holben, B. N., Goloub, P., Cuevas-Agulló, E., Wang, H., Zheng, Y., Zhao, H. and Zhang, X.: Large contribution of meteorological factors to inter-decadal changes in regional aerosol optical depth, Atmos. Chem. 655 Phys., 19(16), 10497–10523, doi:10.5194/ACP-19-10497-2019, 2019a.

Che, H., Yang, L., Liu, C., Xia, X., Wang, Y., Wang, H., Wang, H., Lu, X. and Zhang, X.: Long-term validation of MODIS C6 and C6.1 Dark Target aerosol products over China using CARSNET and AERONET, Chemosphere, 236, 124268, doi:10.1016/J.CHEMOSPHERE.2019.06.238, 2019b.

Che, H., Xia, X., Zhao, H., Dubovik, O., Holben, B. N., Goloub, P., Cuevas-Agulló, E., Estelles, V., Wang, Y., Zhu, J., Qi, B., 660 Gong, W., Yang, H., Zhang, R., Yang, L., Chen, J., Wang, H., Zheng, Y., Gui, K., Zhang, X. and Zhang, X.: Spatial distribution of aerosol microphysical and optical properties and direct radiative effect from the China Aerosol Remote Sensing Network, Atmos. Chem. Phys., 19(18), 11843–11864, doi:10.5194/ACP-19-11843-2019, 2019c.

Cuevas, E., Romero-Campos, P. M., Kouremeti, N., Kazadzis, S., Räisänen, P., García, R. D., Barreto, A., Guirado-Fuentes, C., Ramos, R., Toledano, C., Almansa, F. and Gröbner, J.: Aerosol optical depth comparison between GAW-PFR and 665 AERONET-Cimel radiometers from long-term (2005-2015) 1 min synchronous measurements, Atmos. Meas. Tech., 12(8), 4309–4337, doi:10.5194/AMT-12-4309-2019, 2019.

Dubovik, O. and King, M. D.: A flexible inversion algorithm for retrieval of aerosol optical properties from Sun and sky radiance measurements, J. Geophys. Res. Atmos., 105(D16), 20673–20696, doi:10.1029/2000JD900282, 2000.

Dubovik, O., Smirnov, A., Holben, B. N., King, M. D., Kaufman, Y. J., Eck, T. F. and Slutsker, I.: Accuracy assessments of 670 aerosol optical properties retrieved from Aerosol Robotic Network (AERONET) Sun and sky radiance measurements, J. Geophys. Res. Atmos., 105(D8), 9791–9806, doi:10.1029/2000JD900040, 2000.

Dubovik, O., Holben, B., Eck, T. F., Smirnov, A., Kaufman, Y. J., King, M. D., Tanré, D. and Slutsker, I.: Variability of Absorption and Optical Properties of Key Aerosol Types Observed in Worldwide Locations, J. Atmos. Sci., 59(3), 590–608, doi:10.1175/1520-0469(2002)059, 2002.

675 Dubovik, O., Sinyuk, A., Lapyonok, T., Holben, B. N., Mishchenko, M., Yang, P., Eck, T. F., Volten, H., Muñoz, O., Veihelmann, B., van der Zande, W. J., Leon, J. F., Sorokin, M. and Slutsker, I.: Application of spheroid models to account for aerosol particle nonsphericity in remote sensing of desert dust, J. Geophys. Res. Atmos., 111(D11), 11208, doi:10.1029/2005JD006619, 2006.

Eck, T. F., Holben, B. N., Reid, J. S., Dubovik, O., Smirnov, A., O'Neill, N. T., Slutsker, I. and Kinne, S.: Wavelength
680 dependence of the optical depth of biomass burning, urban, and desert dust aerosols, J. Geophys. Res. Atmos., 104(D24), 31333–31349, doi:10.1029/1999JD900923, 1999.

Estellés, V., Campanelli, M., Utrillas, M. P., Expósito, F. and Martínez-Lozano, J. A.: Comparison of AERONET and SKYRAD4.2 inversion products retrieved from a Cimel CE318 sunphotometer, Atmos. Meas. Tech., 5(3), 569–579, doi:10.5194/AMT-5-569-2012, 2012.

685 Garay, M. J., Kalashnikova, O. V. and Bull, M. A.: Development and assessment of a higher-spatial-resolution (4.4 km) MISR aerosol optical depth product using AERONET-DRAGON data, Atmos. Chem. Phys., 17(8), 5095–5106, doi:10.5194/ACP-17-5095-2017, 2017.

García, O. E., Díaz, A. M., Expósito, F. J., Díaz, J. P., Dubovik, O., Dubuisson, P., Roger, J.-C., Eck, T. F., Sinyuk, A., Derimian, Y., Dutton, E. G., Schafer, J. S., Holben, B. N. and García, C. A.: Validation of AERONET estimates of
690 atmospheric solar fluxes and aerosol radiative forcing by ground-based broadband measurements, J. Geophys. Res. Atmos., 113(D21), doi:10.1029/2008JD010211, 2008.

García, O. E., Díaz, J. P., Expósito, F. J., Díaz, A. M., Dubovik, O., Derimian, Y., Dubuisson, P. and Roger, J. C.: Shortwave radiative forcing and efficiency of key aerosol types using AERONET data, Atmos. Chem. Phys., 12(11), 5129–5145, doi:10.5194/ACP-12-5129-2012, 2012.

695 Goloub, P., Li, Z., Dubovik, O., Blarel, L., Podvin, T., Jankowiak, I., Lecoq, R., Deroo, C., Chatenet, B., Morel, J. P., Cuevas, E. and Ramos, R.: PHOTONS/AERONET sunphotometer network overview: description, activities, results, https://doi.org/10.1117/12.783171, 6936, 218–232, doi:10.1117/12.783171, 2008.

Gordon, H. R. and Wang, M.: Retrieval of water-leaving radiance and aerosol optical thickness over the oceans with SeaWiFS: a preliminary algorithm, Appl. Opt. Vol. 33, Issue 3, pp. 443-452, 33(3), 443–452, doi:10.1364/AO.33.000443, 1994.

700 Gui, K., Che, H., Chen, Q., Zeng, Z., Liu, H., Wang, Y., Zheng, Y., Sun, T., Liao, T., Wang, H. and Zhang, X.: Evaluation of radiosonde, MODIS-NIR-Clear, and AERONET precipitable water vapor using IGS ground-based GPS measurements over China, Atmos. Res., 197, 461–473, doi:10.1016/J.ATMOSRES.2017.07.021, 2017.

Gui, K., Che, H., Wang, Y., Wang, H., Zhang, L., Zhao, H., Zheng, Y., Sun, T. and Zhang, X.: Satellite-derived PM2.5 concentration trends over Eastern China from 1998 to 2016: Relationships to emissions and meteorological parameters,
705 Environ. Pollut., 247, 1125–1133, doi:10.1016/J.ENVPOL.2019.01.056, 2019.

Gui, K., Che, H., Zheng, Y., Wang, Y., Zhang, L., Zhao, H., Li, L., Zhong, J., Yao, W. and Zhang, X.: Seasonal variability and trends in global type-segregated aerosol optical depth as revealed by MISR satellite observations, Sci. Total Environ., 787, 147543, doi:10.1016/J.SCITOTENV.2021.147543, 2021a.

Gui, K., Che, H., Li, L., Zheng, Y., Zhang, L., Zhao, H., Zhong, J., Yao, W., Liang, Y., Wang, Y. and Zhang, X.: The Significant Contribution of Small-Sized and Spherical Aerosol Particles to the Decreasing Trend in Total Aerosol Optical Depth over Land from 2003 to 2018, Engineering, doi:10.1016/J.ENG.2021.05.017, 2021b.

Gui, K., Che, H., Zheng, Y., Zhao, H., Yao, W., Li, L., Zhang, L., Wang, H., Wang, Y. and Zhang, X.: Three-dimensional climatology, trends, and meteorological drivers of global and regional tropospheric type-dependent aerosols: insights from 13 years (2007–2019) of CALIOP observations, Atmos. Chem. Phys., 21(19), 15309–15336, doi:10.5194/ACP-21-15309-2021, 2021c.

Hansen, J., Sato, M. and Ruedy, R.: Radiative forcing and climate response, J. Geophys. Res. Atmos., 102(D6), 6831–6864, doi:10.1029/96JD03436, 1997.

Hauser, A., Oesch, D. and Foppa, N.: Aerosol optical depth over land: Comparing AERONET, AVHRR and MODIS, Geophys. Res. Lett., 32(17), 1–4, doi:10.1029/2005GL023579, 2005.

Holben, B. N., Eck, T. F., Slutsker, I., Tanré, D., Buis, J. P., Setzer, A., Vermote, E., Reagan, J. A., Kaufman, Y. J., Nakajima, T., Lavenu, F., Jankowiak, I. and Smirnov, A.: AERONET—A Federated Instrument Network and Data Archive for Aerosol Characterization, Remote Sens. Environ., 66(1), 1–16, doi:10.1016/S0034-4257(98)00031-5, 1998.

Holben, B. N., Tanré, D., Smirnov, A., Eck, T. F., Slutsker, I., Abuhassan, N., Newcomb, W. W., Schafer, J. S., Chatenet, B., Lavenu, F., Kaufman, Y. J., Castle, J. Vande, Setzer, A., Markham, B., Clark, D., Frouin, R., Halthore, R., Karneli, A., O'Neill, N. T., Pietras, C., Pinker, R. T., Voss, K. and Zibordi, G.: An emerging ground-based aerosol climatology: Aerosol optical depth from AERONET, J. Geophys. Res. Atmos., 106(D11), 12067–12097, doi:10.1029/2001JD900014, 2001.

Hsu, N. C., Herman, J. R., Torres, O., Holben, B. N., Tanre, D., Eck, T. F., Smirnov, A., Chatenet, B. and Lavenu, F.: Comparisons of the TOMS aerosol index with Sun-photometer aerosol optical thickness: Results and applications, J. Geophys. Res. Atmos., 104(D6), 6269–6279, doi:10.1029/1998JD200086, 1999.

Huang, D., Li, X., Zhang, Y. and Zhang, Q. Novel high-precision full autocontrol multi-waveband sun photometer, Journal of Applied Optics, 40(1), doi: 10.5768/JAO201940.0105001, 2019. (In Chinese)

Kazadzis, S., Kouremeti, N., Nyeki, S., Gröbner, J. and Wehrli, C.: The World Optical Depth Research and Calibration Center (WORCC) quality assurance and quality control of GAW-PFR AOD measurements, Geosci. Instrumentation, Methods Data Syst., 7(1), 39–53, doi:10.5194/GI-7-39-2018, 2018.

Kim, M. H., Omar, A. H., Tackett, J. L., Vaughan, M. A., Winker, D. M., Trepte, C. R., Hu, Y., Liu, Z., Poole, L. R., Pitts, M. C., Kar, J. and Magill, B. E.: The CALIPSO version 4 automated aerosol classification and lidar ratio selection algorithm, Atmos. Meas. Tech., 11(11), 6107–6135, doi:10.5194/AMT-11-6107-2018, 2018.

Letu, H., Shi, J., Li, M., Wang, T., Shang, H., Lei, Y., Ji, D., Wen, J., Yang, K. and Chen, L.: A review of the estimation of

740   downward surface shortwave radiation based on satellite data: Methods, progress and problems, Sci. China Earth Sci. 2020 636, 63(6), 774–789, doi:10.1007/S11430-019-9589-0, 2020a.

Letu, H., Yang, K., Nakajima, T. Y., Ishimoto, H., Nagao, T. M., Riedi, J., Baran, A. J., Ma, R., Wang, T., Shang, H., Khatri, P., Chen, L., Shi, C. and Shi, J.: High-resolution retrieval of cloud microphysical properties and surface solar radiation using Himawari-8/AHI next-generation geostationary satellite, Remote Sens. Environ., 239, 111583,

745   doi:10.1016/J.RSE.2019.111583, 2020b.

Levy, R. C., Remer, L. A., Kleidman, R. G., Mattoo, S., Ichoku, C., Kahn, R. and Eck, T. F.: Global evaluation of the Collection 5 MODIS dark-target aerosol products over land, Atmos. Chem. Phys., 10(21), 10399–10420, doi:10.5194/ACP-10-10399-2010, 2010.

Li, J., Jia, L., Xu, W., and Wei, H. Comparison Certification and Error Analysis of Atmospheric Optical Parameters Measured

750   by DTF Sun-Photometer, Journal of Atmospheric and Environmental Optics, 7(2), doi: 10.3969/j.issn.1673-6141.2012.02.002, 2012. (In Chinese)

Li, L., Che, H., Derimian, Y., Dubovik, O., Luan, Q., Li, Q., Huang, X., Zhao, H., Gui, K., Zheng, Y., An, L., Sun, T. and Liang, Y.: Climatology of Fine and Coarse Mode Aerosol Optical Thickness Over East and South Asia Derived From POLDER/PARASOL Satellite, J. Geophys. Res. Atmos., 125(16), e2020JD032665, doi:10.1029/2020JD032665, 2020a.

755 Li, L., Che, H., Derimian, Y., Dubovik, O., Schuster, G. L., Chen, C., Li, Q., Wang, Y., Guo, B. and Zhang, X.: Retrievals of fine mode light-absorbing carbonaceous aerosols from POLDER/PARASOL observations over East and South Asia, Remote Sens. Environ., 247, 111913, doi:10.1016/J.RSE.2020.111913, 2020b.

Liang, Y., Che, H., Gui, K., Zheng, Y., Yang, X., Li, X., Liu, C., Sheng, Z., Sun, T. and Zhang, X.: Impact of Biomass Burning in South and Southeast Asia on Background Aerosol in Southwest China, Aerosol Air Qual. Res., 19(5), 1188–1204,

760   doi:10.4209/AAQR.2018.08.0324, 2019.

Ma, Y., Jin, Y., Zhang, M., Gong, W., Hong, J., Jin, S., Shi, Y., Zhang, Y. and Liu, B.: Aerosol optical properties of haze episodes in eastern China based on remote-sensing observations and WRF-Chem simulations, Sci. Total Environ., 757, 143784, doi:10.1016/J.SCITOTENV.2020.143784, 2021.

Miao, Y., Li, J., Miao, S., Che, H., Wang, Y., Zhang, X., Zhu, R. and Liu, S.: Interaction Between Planetary Boundary Layer

765   and PM2.5 Pollution in Megacities in China: a Review, Curr. Pollut. Reports 2019 54, 5(4), 261–271, doi:10.1007/S40726-019-00124-5, 2019.

Miao, Y., Che, H., Zhang, X. and Liu, S.: Integrated impacts of synoptic forcing and aerosol radiative effect on boundary layer and pollution in the Beijing-Tianjin-Hebei region, China, Atmos. Chem. Phys., 20(10), 5899–5909, doi:10.5194/ACP-20-5899-2020, 2020.

770 Miao, Y., Che, H., Zhang, X. and Liu, S.: Relationship between summertime concurring PM2.5 and O3 pollution and boundary layer height differs between Beijing and Shanghai, China, Environ. Pollut., 268, 115775, doi:10.1016/J.ENVPOL.2020.115775, 2021.

Nakajima, T., Campanelli, M., Che, H., Estellés, V., Irie, H., Kim, S. W., Kim, J., Liu, D., Nishizawa, T., Pandithurai, G., Kumar Soni, V., Thana, B., Tugjsurn, N. U., Aoki, K., Go, S., Hashimoto, M., Higurashi, A., Kazadzis, S., Khatri, P., Kouremeti, N., Kudo, R., Marenco, F., Momoi, M., Ningombam, S. S., Ryder, C. L., Uchiyama, A. and Yamazaki, A.: An overview of and issues with sky radiometer technology and SKYNET, Atmos. Meas. Tech., 13(8), 4195–4218, doi:10.5194/amt-13-4195-2020, 2020.

Ningombam, S. S., Larson, E. J. L., Dumka, U. C., Estellés, V., Campanelli, M. and Steve, C.: Long-term (1995–2018) aerosol optical depth derived using ground based AERONET and SKYNET measurements from aerosol aged-background sites, Atmos. Pollut. Res., 10(2), 608–620, doi:10.1016/J.APR.2018.10.008, 2019.

Ningombam, S. S., Song, H. J., Mugil, S. K., Dumka, U. C., Larson, E. J. L., Kumar, B. and Sagar, R.: Evaluation of fractional clear sky over potential astronomical sites, Mon. Not. R. Astron. Soc., 507(3), 3745–3760, doi:10.1093/MNRAS/STAB1971, 2021.

Sayer, A. M., Hsu, N. C., Bettenhausen, C., Jeong, M. J., Holben, B. N. and Zhang, J.: Global and regional evaluation of over-land spectral aerosol optical depth retrievals from SeaWiFS, Atmos. Meas. Tech., 5(7), 1761–1778, doi:10.5194/AMT-5-1761-2012, 2012.

Stier, P., Feichter, J., Kinne, S., Kloster, S., Vignati, E., Wilson, J., Ganzeveld, L., Tegen, I., Werner, M., Balkanski, Y., Schulz, M., Boucher, O., Minikin, A. and Petzold, A.: The aerosol-climate model ECHAM5-HAM, Atmos. Chem. Phys., 5(4), 1125–1156, doi:10.5194/ACP-5-1125-2005, 2005.

Stowe, L. L., Ignatov, A. M. and Singh, R. R.: Development, validation, and potential enhancements to the second-generation operational aerosol product at the National Environmental Satellite, Data, and Information Service of the National Oceanic and Atmospheric Administration, J. Geophys. Res. Atmos., 102(D14), 16923–16934, doi:10.1029/96JD02132, 1997.

Tao, R., Che, H., Chen, Q., Wang, Y., Sun, J., Zhang, X., Lu, S., Guo, J., Wang, H. and Zhang, X.: Development of an integrating sphere calibration method for Cimel sunphotometers in China aerosol remote sensing network, Particuology, 13(1), 88–99, doi:10.1016/J.PARTIC.2013.04.009, 2014.

Wang, H., Easter, R. C., Rasch, P. J., Wang, M., Liu, X., Ghan, S. J., Qian, Y., Yoon, J.-H., Ma, P.-L. and Vinoj, V.: Sensitivity of remote aerosol distributions to representation of cloud–aerosol interactions in a global climate model, Geosci. Model Dev., 6(3), 765–782, doi:10.5194/GMD-6-765-2013, 2013.

Wang, P., Che, H., Zhang, X., Song, Q., Wang, Y., Zhang, Z., Dai, X. and Yu, D.: Aerosol optical properties of regional background atmosphere in Northeast China, Atmos. Environ., 44(35), 4404–4412, doi:10.1016/J.ATMOSENV.2010.07.043, 2010.

Wei, J., Li, Z., Peng, Y. and Sun, L.: MODIS Collection 6.1 aerosol optical depth products over land and ocean: validation and comparison, Atmos. Environ., 201, 428–440, doi:10.1016/J.ATMOSENV.2018.12.004, 2019.

Xia, X., Che, H., Zhu, J., Chen, H., Cong, Z., Deng, X., Fan, X., Fu, Y., Goloub, P., Jiang, H., Liu, Q., Mai, B., Wang, P., Wu, Y., Zhang, J., Zhang, R. and Zhang, X.: Ground-based remote sensing of aerosol climatology in China: Aerosol optical

properties, direct radiative effect and its parameterization, Atmos. Environ., 124, 243–251, doi:10.1016/J.ATMOSENV.2015.05.071, 2016.

Xia, X., Che, H., Shi, H., Chen, H., Zhang, X., Wang, P., Goloub, P. and Holben, B.: Advances in sunphotometer-measured aerosol optical properties and related topics in China: Impetus and perspectives, Atmos. Res., 249, 105286, doi:10.1016/J.ATMOSRES.2020.105286, 2021.

Xing, C., Liu, C., Hu, Q., Fu, Q., Lin, H., Wang, S., Su, W., Wang, W., Javed, Z. and Liu, J.: Identifying the wintertime sources of volatile organic compounds (VOCs) from MAX-DOAS measured formaldehyde and glyoxal in Chongqing, southwest China, Sci. Total Environ., 715, doi:10.1016/j.scitotenv.2019.136258, 2020.

Xing, C., Liu, C., Wu, H., Lin, J., Wang, F., Wang, S. and Gao, M.: Ground-based vertical profile observations of atmospheric composition on the Tibetan Plateau (2017–2019), Earth Syst. Sci. Data, 13(10), 4897–4912, doi:10.5194/ESSD-13-4897-2021, 2021a.

Xing, C., Liu, C., Hu, Q., Fu, Q., Wang, S., Lin, H., Zhu, Y., Wang, S., Wang, W., Javed, Z., Ji, X. and Liu, J.: Vertical distributions of wintertime atmospheric nitrogenous compounds and the corresponding OH radicals production in Leshan, southwest China, J. Environ. Sci. (China), 105, 44–55, doi:10.1016/j.jes.2020.11.019, 2021b.

Yu, J., Che, H., Chen, Q., Xia, X., Zhao, H., Wang, H., Wang, Y., Zhang, X. and Shi, G.: Investigation of Aerosol Optical Depth (AOD) and Ångström Exponent over the Desert Region of Northwestern China Based on Measurements from the China Aerosol Remote Sensing Network (CARSNET), Aerosol Air Qual. Res., 15(5), 2024–2036, doi:10.4209/AAQR.2014.12.0326, 2015.

Zhang, L., Zhao, T., Gong, S., Kong, S., Tang, L., Liu, D., Wang, Y., Jin, L., Shan, Y., Tan, C., Zhang, Y. and Guo, X.: Updated emission inventories of power plants in simulating air quality during haze periods over East China, Atmos. Chem. Phys., 18(3), 2065–2079, doi:10.5194/ACP-18-2065-2018, 2018.

Zhang, L., Gong, S., Zhao, T., Zhou, C., Wang, Y., Li, J., Ji, D., He, J., Liu, H., Gui, K., Guo, X., Gao, J., Shan, Y., Wang, H., Wang, Y., Che, H. and Zhang, X.: Development of WRF/CUACE v1.0 model and its preliminary application in simulating air quality in China, Geosci. Model Dev., 14(2), 703–718, doi:10.5194/GMD-14-703-2021, 2021a.

Zhang, X., Li, L., Chen, C., Chen, X., Dubovik, O., Derimian, Y., Gui, K., Zheng, Y., Zhao, H., Zhang, L., Guo, B., Wang, Y., Holben, B., Che, H. and Zhang, X.: Validation of the aerosol optical property products derived by the GRASP/Component approach from multi-angular polarimetric observations, Atmos. Res., 263, 105802, doi:10.1016/J.ATMOSRES.2021.105802, 2021b.

Zhao, C., Yang, Y., Fan, H., Huang, J., Fu, Y., Zhang, X., Kang, S., Cong, Z., Letu, H. and Menenti, M.: Aerosol characteristics and impacts on weather and climate over the Tibetan Plateau, Natl. Sci. Rev., 7(3), 492–495, doi:10.1093/NSR/NWZ184, 2020.

Zhao, F., Liu, C., Cai, Z., Liu, X., Bak, J., Kim, J., Hu, Q., Xia, C., Zhang, C., Sun, Y., Wang, W. and Liu, J.: Ozone profile retrievals from TROPOMI: Implication for the variation of tropospheric ozone during the outbreak of COVID-19 in China, Sci. Total Environ., 764, 142886, doi:10.1016/J.SCITOTENV.2020.142886, 2021a.

Zhao, H., Che, H., Xia, X., Wang, Y., Wang, H., Wang, P., Ma, Y., Yang, H., Liu, Y., Wang, Y., Gui, K., Sun, T., Zheng, Y. and Zhang, X.: Multiyear Ground-Based Measurements of Aerosol Optical Properties and Direct Radiative Effect Over Different Surface Types in Northeastern China, J. Geophys. Res. Atmos., 123(24), 13,887-13,916, doi:10.1029/2018JD029141, 2018.

845 Zhao, H., Gui, K., Ma, Y., Wang, Y., Wang, Y., Wang, H., Zheng, Y., Li, L., Zhang, L., Che, H. and Zhang, X.: Climatological variations in aerosol optical depth and aerosol type identification in Liaoning of Northeast China based on MODIS data from 2002 to 2019, Sci. Total Environ., 781, 146810, doi:10.1016/J.SCITOTENV.2021.146810, 2021b.

Zhao, H., Gui, K., Ma, Y., Wang, Y., Wang, Y., Wang, H., Zheng, Y., Li, L., Zhang, L., Che, H. and Zhang, X.: Climatology and trends of aerosol optical depth with different particle size and shape in northeast China from 2001 to 2018, Sci. Total

850 Environ., 763, 142979, doi:10.1016/J.SCITOTENV.2020.142979, 2021c.

Zheng, Y., Che, H., Xia, X., Wang, Y., Wang, H., Wu, Y., Tao, J., Zhao, H., An, L., Li, L., Gui, K., Sun, T., Li, X., Sheng, Z., Liu, C., Yang, X., Liang, Y., Zhang, L., Liu, C., Kuang, X., Luo, S., You, Y. and Zhang, X.: Five-year observation of aerosol optical properties and its radiative effects to planetary boundary layer during air pollution episodes in North China: Intercomparison of a plain site and a mountainous site in Beijing, Sci. Total Environ., 674, 140–158,

855 doi:10.1016/J.SCITOTENV.2019.03.418, 2019.

Zheng, Y., Che, H., Xia, X., Wang, Y., Yang, L., Chen, J., Wang, H., Zhao, H., Li, L., Zhang, L., Gui, K., Yang, X., Liang, Y. and Zhang, X.: Aerosol optical properties and its type classification based on multiyear joint observation campaign in north China plain megalopolis, Chemosphere, 273, 128560, doi:10.1016/J.CHEMOSPHERE.2020.128560, 2021.

Zhuang, B., Wang, T., Liu, J., Li, S., Xie, M., Han, Y., Chen, P., Hu, Q., Yang, X. Q., Fu, C. and Zhu, J.: The surface aerosol

860 optical properties in the urban area of Nanjing, west Yangtze River Delta, China, Atmos. Chem. Phys., 17(2), 1143–1160, doi:10.5194/ACP-17-1143-2017, 2017.